Crashworthiness design of AlSi10Mg lattice structures through heat treatments

International Journal of Mechanical Sciences 324 (2026) 111789

Contents lists available at ScienceDirect

International Journal of Mechanical Sciences

journal homepage: www.elsevier.com/locate/ijmecsci

Crashworthiness design of AlSi10Mg lattice structures through heat treatments

Alessandro Benelli [a,c,*], Carlo Boursier Niutta [b,c], Andrea Tridello [b,c]

[a] Department of Applied Science and Technology, Politecnico di Torino, 10129 Turin, Italy
[b] Department of Mechanical and Aerospace Engineering, Politecnico di Torino, 10129 Turin, Italy
[c] Inter-Departmental Multi-Disciplinary Research Centre J-TECH @PoliTO, Turin, Italy

ARTICLE INFO

Keywords:
Additive manufacturing
Impact mechanics
AlSi10Mg
Lattice octet-truss
Heat treatment
Crashworthiness

ABSTRACT

This study investigates the process-structure-property relationship of LPBF AlSi10Mg octet-truss lattices for crash-absorption applications. The main novelty is the use of low-temperature post-process heat treatments as explicit design variables to tune crash performance without changing the lattice geometry.

Lattice specimens were tested in the as-built condition and after two heat treatments, at 200 °C (HT-200) and at 300 °C (HT-300), under quasi-static compression and low-velocity impact loading (4 and 8 m/s). The results show that heat treatment strongly affects deformation mode and energy-absorption capability. HT-300 promotes a smoother and more stable collapse, significantly increases specific energy absorption, and reduces force peaks, whereas HT-200 provides limited benefits compared with the as-built condition.

Microstructural analyses indicate that the improved response is associated with thermally induced changes that increase ductility and enable more homogeneous plastic deformation. A finite element model, calibrated and validated against the experiments across strain rates, was then used to design a lattice-based crash box for automotive applications. The proposed solution meets the crash-energy target of a segment C vehicle while achieving >40% mass reduction compared with a conventional crash tube. At the component level, this corresponds to an increase in specific energy absorption of 67%, passing from 11.5 kJ/kg for the reference crash tube to 20.16 kJ/kg for the proposed lattice absorber.

Overall, the study demonstrates that heat treatment can be used as a geometry-free design lever to tailor the crashworthiness of additively manufactured lattice structures.

1. Introduction

In recent years, the rapid diffusion of Additive Manufacturing (AM) has enabled the production of components with complex geometries that are difficult or impossible to fabricate using traditional processes [1–4]. This design freedom is a key advantage of AM over conventional manufacturing [1,2]. As a consequence, previously under-used design methodologies can now be reliably leveraged to optimize component performance and, for example, reduce weight without compromising safety. A prominent example is topology optimization, which, when combined with AM, enables the design of lightweight, high-performance components [5–7]. In parallel, growing interest is devoted to metamaterials and lattice structures, with recent studies showing a rapid shift from conventional strut-based lattices toward plate-based, thin-plate and TPMS-derived architectures capable of improved stiffness-to-weight ratio and energy absorption [8–14]. Lattices are obtained by spatially replicating a unit cell whose geometric features can be tuned to meet target performance. They have been used, for instance, for acoustic applications and vibration damping [15–17] and, importantly, for crashworthiness and energy absorption [18,19]. Recent work on LPBF AlSi10Mg architected materials further confirms that topology class, including strut-, plate- and TPMS-based designs, strongly influences deformation stability and specific energy absorption under compression [20–22]. The design of the unit cell is therefore crucial to tailor properties for the intended application: while relative density primarily controls mass, the cell geometry governs the mechanical response, often distinguishing between bending-dominated and stretch-dominated behaviours, thus enabling lightweight yet robust structures [23,24]. In recent years, both topology optimization and Machine Learning approaches have been employed to navigate such high-dimensional design

E-mail address: alessandro.benelli@polito.it (A. Benelli).
* Corresponding author at: Department of Applied Science and Technology, Politecnico di Torino, 10129 Turin, Italy.

https://doi.org/10.1016/j.ijmecsci.2026.111789
Received 22 December 2025; Received in revised form 30 April 2026; Accepted 30 May 2026
Available online 1 June 2026

spaces [6,25–27]

Despite these advantages, designing lattice structures for real components remains challenging. Direct simulation of lattice behaviour is computationally expensive due to the fine cell length scales and the large number of repeating units in full-scale parts; multiscale and homogenization strategies are therefore often required [28–35]. Moreover, geometric deviations and imperfections, e.g., defects and surface roughness, inevitably introduced during manufacturing, degrade the ideal (theoretical) mechanical performance and must be considered in the design process [36–39]. Recent studies on LPBF AlSi10Mg further highlighted that internal defect morphology, anisotropy and architecture-dependent deformation localization can substantially alter the compressive and failure response of architected materials, thus motivating defect-aware and process-informed design strategies [40–42]. These aspects highlight the importance of the process-structure-property relationship in AM: process parameters and post-treatments strongly influence the properties and failure modes of lattice structures [2,43,44]. This is particularly relevant for AlSi10Mg lattices, where recent studies have shown that architecture class, local geometric tuning and manufacturing quality interact strongly in determining both load-bearing capability and energy-absorption stability [41,45]. Recent studies on hollow-strut metallic lattices further showed that mass efficiency, energy absorption and collapse stability can be improved by redistributing material within the struts while preserving the overall lattice topology. This is particularly relevant to the present study, as it represents a geometry-preserving tuning strategy complementary to the heat-treatment-based approach adopted here [45–49]. From this perspective, post-process treatments can be regarded as design variables to tune the mechanical response without complicating the unit-cell geometry [50,51].

Existing research often focuses on optimizing the unit cell to achieve target properties [52–54]. More recent studies on LPBF AlSi10Mg have also shown that heat treatment and post-processing can be exploited to modify not only strength and ductility, but also collapse stability, stress fluctuations and specific energy absorption, both in conventional lattices and in more recent TPMS- or plate-based architectures [55,56]. For example, Fiocchi et al. [44] showed that residual-stress relief is a dominant factor for achieving smooth quasi-static compression and improved energy absorption in AlSi10Mg lattices. Tang et al. [57] fabricated uniform and graded diamond lattices (USK/USH/GSK/GSH) in AlSi10Mg by SLM and observed that heat treatments (solution temperatures between 25 and 300 °C) alter failure modes, for GSH at 300 °C, from layer-by-layer fracture to 45° shear. Jam et al. [58] tested Ti-21S octet-truss lattices (as-built vs. direct ageing at 590 °C for 8 h) and reported elimination of strain softening and a transition from bending-dominated to stretch-dominated behaviour. Jin et al. [59] studied Ti-6Al-4 V BCC (bending-dominated) and FCC (stretch-dominated) lattices subjected to heat treatments (750–1050 °C, including HIP), finding BCC markedly more sensitive to heat-treatment conditions than FCC. Li et al. [60] investigated AlSi10Mg lattices under AA, SHT, and SHT+AA (SHA), showing SHA (with Tmax≈550 °C) delivered the best compressive properties and a shift from brittle to ductile fracture with stable deformation. Recent dynamic and crash-oriented investigations further suggest that these effects are highly relevant for real energy-management applications, since constitutive calibration under dynamic loading and lattice-reinforced thin-walled absorbers can markedly influence crashworthiness metrics at structural scale [61,62].

The present paper investigates the process-structure-property relationship of AlSi10Mg octet-truss lattice structures produced by Laser Powder Bed Fusion (L-PBF) for crash-absorbing applications. In this study, heat treatments are designed and used as explicit tuning variables of the lattice response, and the correspondence between quasi-static bulk material tests and lattice behaviour is assessed.

The octet-truss architecture, being stretch-dominated, is generally suited to lightweight applications where high stiffness/strength and efficient load transfer are required [23–25]. At the same time, it is important to acknowledge that bending-dominated lattices often exhibit longer and more stable collapse plateaus and may provide higher specific energy absorption at comparable relative density [63–66]. In the present study, the octet-truss was therefore not selected as a universally optimal crash topology, but rather as a mechanically well-understood architecture that allows the effect of heat treatment on the process-structure-property relationship to be isolated without the additional complexity introduced by topology changes [67–69]. Within this framework, suitable post-treatments, such as heat treatments, are selected to achieve the desired mechanical response.

In this study, an additively manufactured AlSi10Mg lattice structure is investigated in three conditions: as-built (AB), and after low-temperature heat treatments at 200 °C for 4 h (HT-200) and 300 °C for 2 h (HT-300). The mechanical behaviour is characterised by quasi-static compression tests and dynamic impact tests at 4 m/s and 8 m/s, to assess the combined influence of heat treatment and strain rate on energy absorption, peak force and deformation mode. In parallel, a finite element (FE) model of a lattice-based crash box is developed and compared with a real crash tube to evaluate crashworthiness at the component level.

While recent studies have expanded the literature on crashworthiness and impact resistance of additively manufactured AlSi10Mg architected materials, the use of low-temperature heat treatments as explicit design variables to tune the crash response of octet-truss lattices without changing geometry remains insufficiently clarified [70,71]. The study addresses key open issues by: (i) clarifying the different roles of HT-200 and HT-300 on dynamic energy absorption and collapse mechanism; (ii) quantifying the strain-rate sensitivity of AlSi10Mg lattices; and (iii) demonstrating, via FE simulations, that thermally tuned lattice crash boxes can meet real crash energy targets while achieving significant mass reduction compared with conventional designs.

The paper is organized as follows. Section 2 describes the investigated lattice geometries, the LPBF process, the heat treatments, the microstructural and defect analyses, and the experimental procedures. Section 3 presents the experimental results, with emphasis on microstructural evolution, defect population, and quasi-static and dynamic crushing response. Section 4 discusses the relationship between heat-treatment-induced microstructural changes, deformation modes, failure initiation, and damage evolution, and highlights the implications of the octet-truss topology for crash-oriented design. Section 5 develops and validates the FE model and applies it to the design of a lattice-based automotive crash absorber. Finally, Section 6 summarizes the main findings and discusses their implications for crash-oriented lattice design.

2. Specimen characteristics, material and experimental activity

This section describes the experimental framework adopted to investigate the effect of low-temperature heat treatment on the crash response of LPBF AlSi10Mg octet-truss lattices. It first introduces the specimen geometry, manufacturing route, and heat-treatment schedules, then summarizes the microstructural and defect characterization methods, and finally presents the quasi-static and impact test procedures.

2.1. Lattice structure specimens and heat treatments

Experimental tests have been carried out on AlSi10Mg specimens produced by the Italian company Beam It. Spherical powders have been used for the specimen production, with an average size (D50) of 42 μm and a layer thickness of 30 μm.

A cubic octet truss unit cell, with a nominal diameter of 1.4 mm and a cell side of 8.5 mm, has been considered for specimen production. Two specimens have been tested in this activity: a specimen made of 2 × 2 × 2 cells, i.e., 2 per side, and a specimen made of 3 × 3 × 3 cells, with three

cells per side. Fig. 1 shows the 3 × 3 × 3 lattice structure reconstructed by x-ray computed tomography.

After the specimen production, the specimens have been removed from the building platform. One set of specimens has been tested in the as-built condition, whereas two batches of specimens have undergone two heat treatments, with the following characteristics:

- HT-200: 4 h at a heating temperature of 200 °C with an initial heating ramp of 5°K/min rate and then cooled down in air.
- HT-300: 2 h at a heating temperature of 300 °C, with an initial heating ramp of 5°K/min rate and then cooled down in air.

These two treatments have been carried out in CARBOLITE HTF16/27 furnace (Verder Scientific GmbH and Co. KG, Germany) present in the JTech@PoliTO laboratories. Tensile tests on standard dogbone specimens have been carried out in displacement-controlled mode (crosshead speed of 1 mm/min), with the deformation measured with the Digital Image Correlation (DIC) technique. Table 1 shows the quasi-static properties of the AlSi10Mg specimens, in the investigated conditions. In particular, the Young's modulus E, the tensile strength, σ_u, and the deformation to failure are reported. In the second column, the average deformation to failure assessed by considering a "virtual extensometer" along the gage length is reported (ε_{global}). On the other hand, in the third column, the local deformation where the failure originated is reported (ε_{local}). This last value is of particular relevance in FE modelling, since it is the actual value of deformation that the material can withstand, as detailed in the following Section.

According to Table 1, the Young's modulus is similar for all tested specimens, whereas the tensile strength is dependent on heat treatment. In particular, σ_u is close for the AB and the HT-200 specimens, with limited differences, whereas is significantly smaller for the HT-300 specimen (reduction of 42%). On the other hand, the ductility is significantly larger in HT-300 specimens, with ε_{global} being equal to 10.7% and ε_{local} to 53.7%, about 5 times larger than that of AB and HT-200, which are very close. This increment in ductility is expected to be beneficial for the absorption capability of the lattice structure, since, after the HT-300, the material is capable of locally withstanding very large deformations.

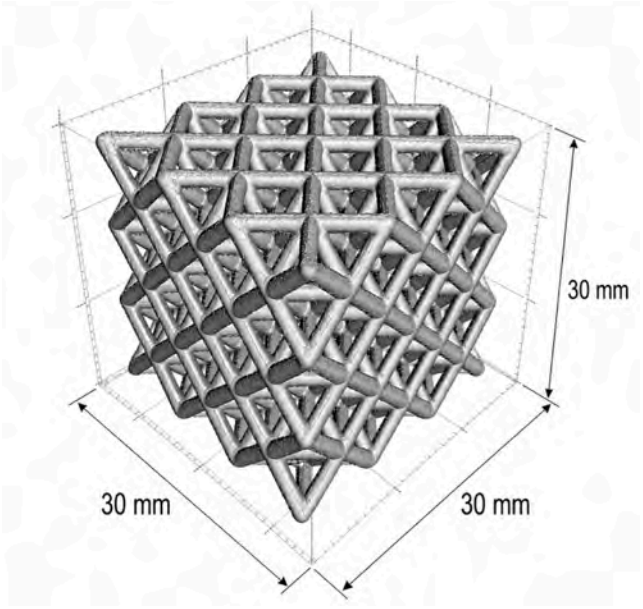

Fig. 1. X-ray computed tomography reconstruction of the 3 × 3 × 3 octet-truss lattice specimen used in this study. The image is provided to document the specimen architecture, unit-cell arrangement, and geometric fidelity of the LPBF-manufactured lattice. The distance between two consecutive major tick in the figure is equal to 10 mm.

Table 1
Quasi-static tensile properties of LPBF AlSi10Mg in the three investigated conditions (AB, HT-200, and HT-300). The table reports Young's modulus, tensile strength, average strain to failure measured over the gauge length by a virtual extensometer, and local strain to failure measured at the failure-initiation region. The distinction between average and local strain is particularly relevant for HT-300, where deformation localizes more strongly before rupture.

Specimen type	E [MPa]	σ_u [MPa]	ε_{global}	ε_{local}
AB	70.5	422	7%	10.4%
HT-200	72.2	425	5%	13.5%
HT-300	59.6	247	10.7%	53.7%

2.2. Microstructural analysis

A thorough analysis of the microstructure and the defect population have been carried out, to verify the influence of the investigated heat treatments and to correlate them with the experimentally assessed mechanical properties.

2.2.1. Grain size analysis by EBSD

To assess the evolution of the microstructure after the heat treatments described in Section 2.1, grain size analysis was performed using Electron Backscatter Diffraction (EBSD). Before EBSD analysis, the specimens were prepared by standard mechanical grinding and polishing on a plane perpendicular to the build direction, followed by a final colloidal silica polish to achieve a mirror-quality surface. After polishing, the specimens were cleaned in an ultrasonic bath containing isopropanol at room temperature to eliminate residual silica particles. EBSD measurements were carried out using an Oxford Instruments AZtec EBSD system integrated into a Tescan MIRA3 (Tescan Group, Brno, CZ) Field Emission Scanning Electron Microscope (FESEM). During the analysis, the sample surface was tilted at 70° relative to the horizontal plane to optimize the signal collection by the EBSD detector. Crystallographic orientation maps were then acquired and processed to determine the grain size distribution and its variation induced by the heat treatments. The parameters used for the analysis are reported in Table 2:

2.2.2. Defect analysis by X-ray computed tomography

The internal defect population within the lattice structure specimens was analyzed using X-ray Computed Tomography (CT), employing the dedicated facilities available at the J-Tech@PoliTO laboratory. The tomography system is equipped with a 300 kV micro-focus X-ray source with a minimum focal spot size of 5 μm and a flat-panel detector with a resolution of 2048 × 2048 pixels. For the acquisition, optimized scanning parameters were selected, operating the system at 170 kV and 100 μA, corresponding to a nominal power of 17 W. The geometrical setup was configured with a source-to-sample distance of 120 mm and a source-to-detector distance of 1000 mm, resulting in a final voxel size of 24 μm. To enhance the image contrast and reduce low-energy noise, a 0.4 mm copper filter was applied to the X-ray beam during acquisition. The tomographic reconstruction was performed using the filtered back-

Table 2
Main acquisition parameters used for the EBSD analysis of the investigated AlSi10Mg specimens.

Parameter	Value
High voltage	20 kV
Beam Intensity	17 pA
Working distance	≈ 15 mm
Magnification	≈ 900x
Dwell time	≈ 12 h
Step size	0.20 μm

projection algorithm implemented in VGStudio MAX 3.5 (Volume Graphics GmbH, Heidelberg, Germany), based on 1600 projections collected during the scan. The reconstructed 3D volumes were subsequently analyzed to detect and characterize internal defects in terms of size, morphology, and spatial distribution.

2.3. Quasi-static and impact experimental tests

Compressive quasi-static and impact tests have been carried out on the specimens with the geometry described in Section 2.1. In particular, quasi-static compressive tests have been carried out on $2 \times 2 \times 2$ specimens and $3 \times 3 \times 3$ specimens by using a Zwick Z050 (Zwick GmbH & Co. KG, Ulm, DE) testing machine, by imposing a crosshead displacement of 1 mm/min. Two repetitions for each type of specimen have been performed. The load has been acquired with a 50 kN load cell. The experimental tests have been also recorded with a Dynolite microscope to assess the failure mode and have been stopped at the onset of densification.

Impact tests have been carried out by using a free-fall drop dart testing machine, FractoVIS (Instron, Norwood, MA, USA). Impact tests have been carried out at two different speed (v_0), namely 4 m/s and 8 m/s, corresponding to 14.4 km/h and 28.8 km/h, respectively. The two impact speeds have been obtained by setting a specific height and weight. This range is of interest in low-velocity impact tests, e.g., crash box, and therefore of interest in practical applications.

3. Experimental results

This section presents the experimental evidence linking heat treatment, microstructural evolution, defect population, and crushing response. The discussion is organized progressively, from microstructure and defects to quasi-static and dynamic mechanical behaviour, in order to clarify how the investigated thermal conditions affect failure mode and energy absorption.

3.1. Microstructural analysis

The EBSD analysis of the AlSi10Mg alloy in the as-built and heat-treated conditions (200 °C and 300 °C) highlights a clear microstructural evolution driven by thermal exposure. The as-built sample exhibits a fine-grained microstructure with a highly heterogeneous crystallographic orientation distribution, as indicated by the random colour distribution in the IPF maps (Fig. 2a). The grain boundary density is high, reflecting the presence of numerous small grains, typical of additively manufactured materials subjected to rapid solidification.

Upon heat treatment at 200 °C, the microstructure undergoes limited grain growth, with slight substructure rearrangement likely associated with recovery phenomena. The grain boundaries remain dense, although a modest reduction is observed (Fig. 2b).

A more pronounced microstructural modification is evident after treatment at 300 °C, where grain coarsening is noticeable, resulting in larger and more equiaxed grains and a lower grain boundary density. A partial development of texture is also suggested by a less random orientation distribution (Fig. 2c).

These qualitative observations are fully supported by the quantitative grain size distributions reported in Fig. 3. The grain size distribution progressively shifts towards larger equivalent diameters with increasing temperature, while maintaining a decreasing trend across all conditions. The obtained trends are comparable to the ones in the literature [72]. Specifically, the as-built sample exhibits a distribution peak between 0.5–0.7 μm, with an average grain size of 0.99 μm and a maximum grain size of approximately 5.2 μm. The sample heat-treated at 200 °C shows a peak between 1.0–1.2 μm, an average grain size of 1.80 μm, and a maximum size close to 8.6 μm. Finally, the sample treated at 300 °C displays a peak between 1.2–1.4 μm, with an average grain size of 2.11 μm and a maximum reaching 8.7 μm. This limited grain coarsening is generally attributed to the strong pinning effect of the Si-rich eutectic and Mg_2Si precipitates on grain boundaries, which restricts grain growth at these relatively low temperatures [73,74]. Low-temperature treatments progressively transform the continuous Si-rich network

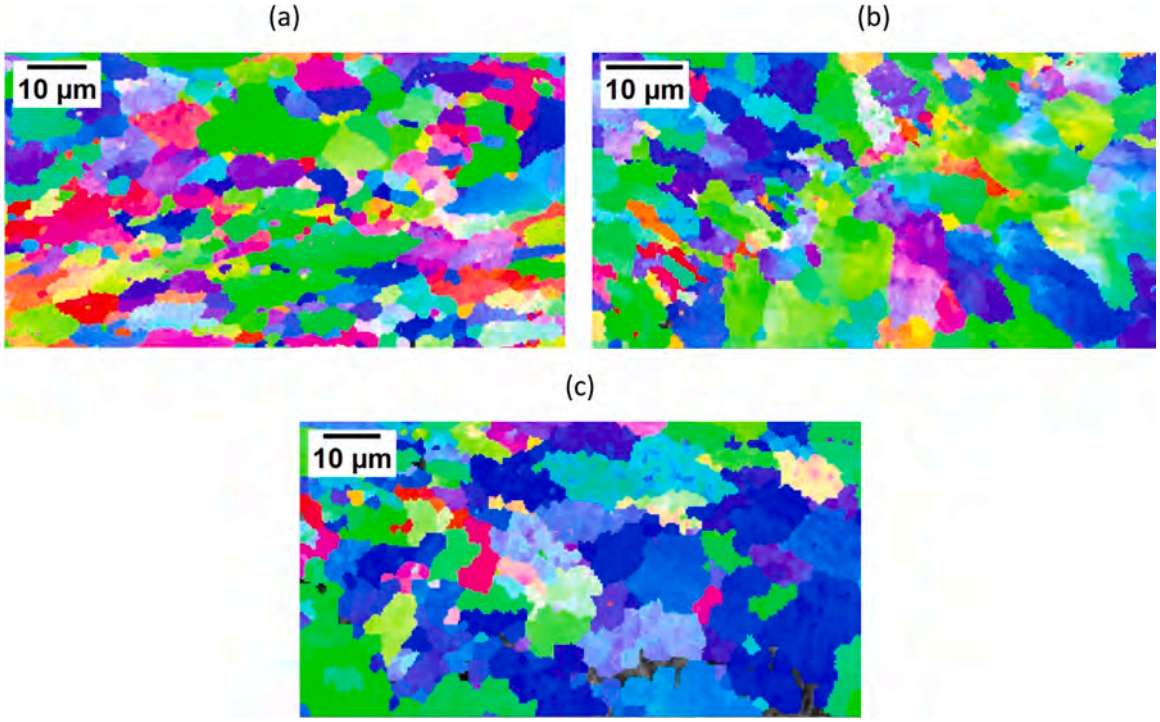

Fig. 2. EBSD inverse pole figure maps of the investigated AlSi10Mg conditions: (a) as-built (AB), (b) HT-200, and (c) HT-300. The maps are used to compare grain morphology and grain-size evolution after heat treatment. A progressive coarsening of the microstructure is observed with increasing treatment temperature, with the most evident grain growth in HT-300.

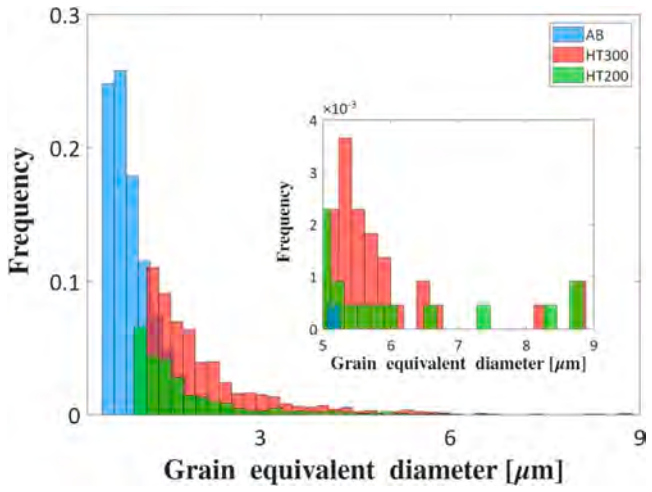

Fig. 3. Grain-size distributions obtained from EBSD analysis for the as-built, HT-200, and HT-300 conditions. The distributions shift progressively toward larger equivalent grain diameters with increasing heat-treatment temperature, confirming limited but measurable grain coarsening after thermal exposure.

surrounding the Al cells into a population of more isolated, rounded Si-rich particles. This fragmentation and spheroidization of the eutectic Si weakens the constraint on dislocation motion, allowing more homogeneous plastic flow and delaying the onset of micro-crack nucleation at the Si/Al interfaces [11]. At the same time, fine Mg_2Si precipitation during the lower-temperature treatment (around 160–200 °C) provides additional strengthening [75,76], whereas approaching 300 °C leads to coarsening of the Si-rich phase and an over-aged condition which further improves ductility but reduces strength, as can be seen from Table 1 [73,74].

3.2. Defect analysis

Defect populations assessed by micro-CT are compared in this section to determine whether defect size changes with the tested heat treatments. Because the two cell sizes show similar trends, only the results for the 3 × 3 × 3 specimens are presented for clarity.

Fig. 4 compares the pore-size distributions in the as-built specimens and in the specimens subjected to the two heat treatments at 200 °C and 300 °C. Across all conditions, the equivalent-diameter distributions are very similar, with a clear mode around 50 −70 μm and an extension up to about 210 μm. In particular, the peak of the AB condition is slightly shifted to the left with respect to the heat-treated specimens. Small differences can be observed in the tail of the distributions, where the AB condition appears to contain a somewhat larger fraction of pores above 150 μm. However, this difference remains limited and should be interpreted with caution, since the overall distributions are very close and rare large defects are still found also in the HT-300 condition. This suggests that the observed differences in the tail are more likely associated with the random occurrence of a small number of large defects than with a systematic heat-treatment-induced change in defect size. The three histograms were constructed using the same bin size for all conditions, so that the comparison is not affected by differences in histogram discretization.

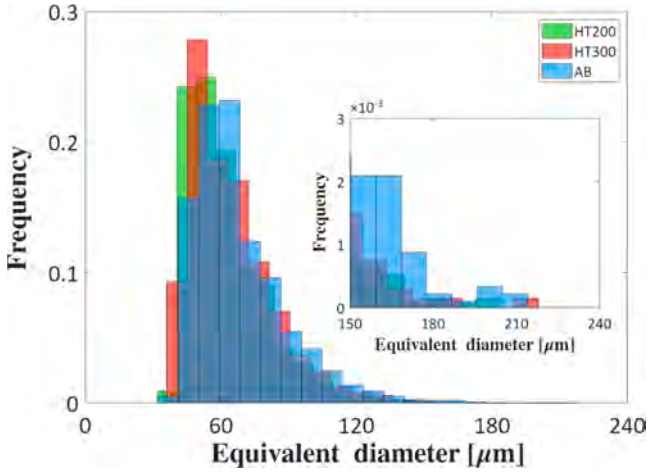

Fig. 4. Equivalent-diameter distributions of internal defects measured by micro-CT for the 3 × 3 × 3 lattice specimens in the as-built, HT-200, and HT-300 conditions. The three distributions are overall very similar, with only limited differences in the tail above about 150 μm, indicating that the investigated heat treatments do not substantially modify the global defect-size distribution.

Fig. 5 shows sphericity as a function of equivalent diameter. In all three samples, sphericity decreases with increasing size, with most defects in the 0.45–0.65 range. Smaller defects exhibit similar sphericity across samples. The as-built and 200 °C specimens follow comparable trends, whereas the 300 °C specimen displays a lower sphericity bound around 0.37. This is consistent with the 3D reconstructions of the largest defects: the largest defects in the as-built and 200 °C samples are highly irregular (Fig. 6a and b), while the largest defect in the 300 °C sample is closer to equiaxed as shown in Fig. 6c.

To provide a more quantitative summary of the defect state, the defect volume fraction and the maximum defect size were also evaluated from the micro-CT scans (Table 3). The values in the table are expressed as mean results since the tomography inspection has been done in all the tested specimens. These measurements confirm that all the investigated conditions exhibit a comparable overall defect population, with only limited differences between heat treatments in terms of global defect content, while the main difference remains associated with the morphology of the largest defects.

3.3. Quasi-static and impact experimental tests

This Section focuses on the mechanical tests carried out to investigate the energy absorption capability of the tested AlSi10Mg specimens. The results of the quasi-static and impact tests are analyzed in Sections 3.3.1 and 3.3.2, respectively, to assess the influence of heat treatments on the compressive response.

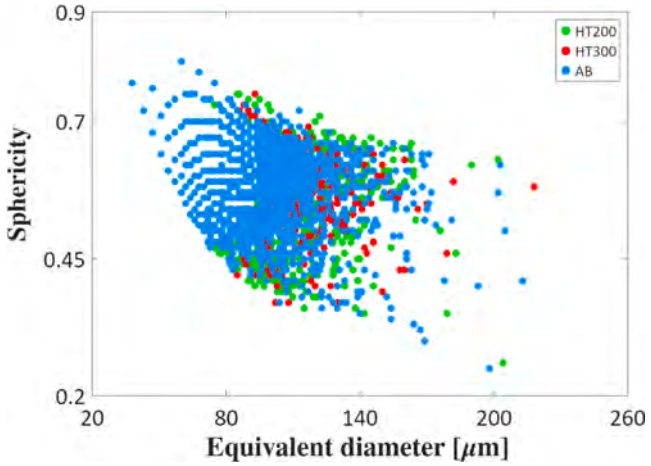

Fig. 5. Defect sphericity as a function of equivalent diameter for the 3 × 3 × 3 lattice specimens in the as-built, HT-200, and HT-300 conditions. In all cases, larger defects tend to be less spherical. The HT-300 condition shows a defect morphology that is, on average, more equiaxed for the largest observed defects.

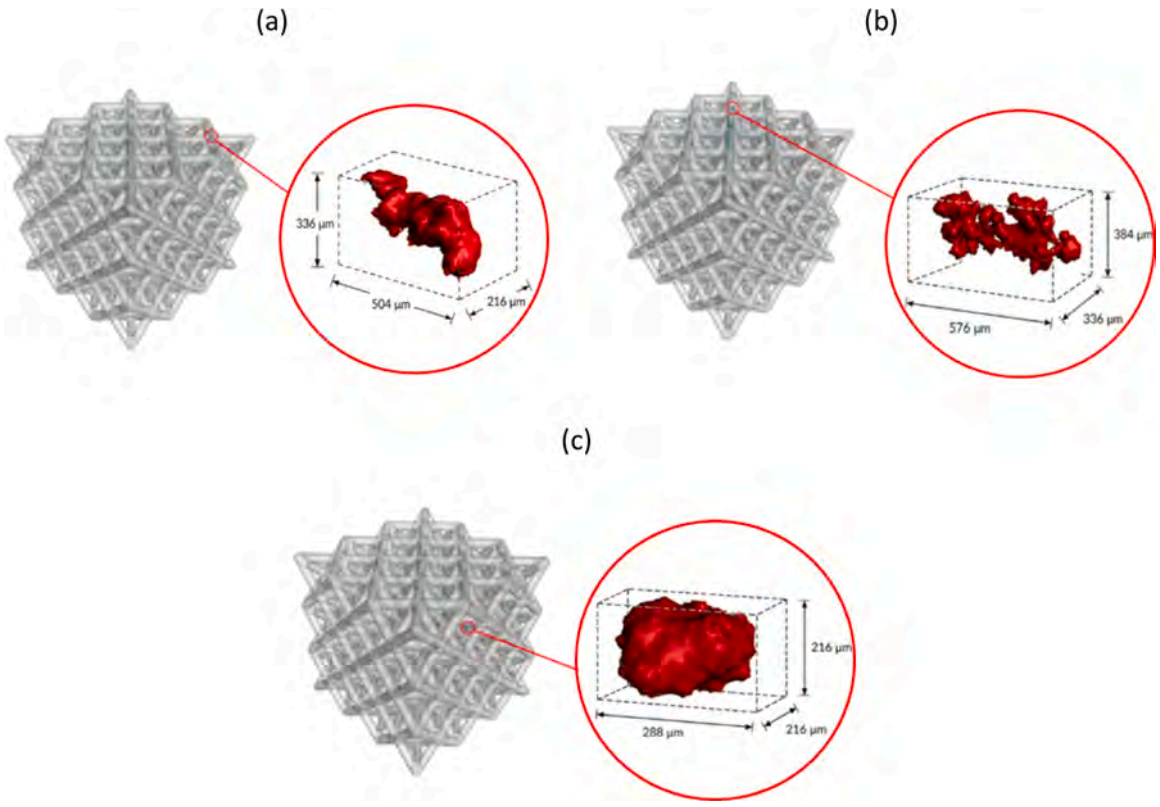

Fig. 6. Enlargement of the biggest defect: a) As built specimen; b) specimen heat treated at 200 °C and c) specimen heat treated at 300 °C. With higher treatment temperature the largest defect tends to be more spherical.

Table 3
Summary of the micro-CT-based defect metrics for the investigated specimens. Reported quantities include mean defect sphericity, defect volume fraction, mean maximum equivalent diameter, and qualitative morphology of the largest detected defect.

Specimen	Mean sphericity index	Defect volume ratio [%]	Mean maximum equivalent diameter [µm]	Largest defect morphology
AB	0.638	0.03	213	Irregular
HT-200	0.653	0.04	204	Irregular
HT-300	0.656	0.02	218	More equiaxed

3.3.1. *Quasi-static tests*

Quasi-static compression tests have been carried out on 2 × 2 × 2 and 3 × 3 × 3 specimens. Fig. 7 compares the Force - displacement curves for the 2 × 2 × 2 specimen (Fig. 7a) and for the 3 × 3 × 3 specimens (Fig. 7b). The tests have been stopped before the densification.

According to Fig. 7a and by considering the 2 × 2 × 2 specimens, the heat treatment has a significant influence on the trend of the force-displacement curves. Indeed, the AB and the HT 200 specimens have a similar trend, with the as-built specimens showing the highest peak. However, the difference is quite limited and close to 9%. Similarly, the displacement at failure and before the densification phase is very close. These curves, moreover, show a rapid drop of the force after the peak force is reached. On the other hand, the HT300 specimens show a significantly smaller peak force, which is about 60% of the peak stress of the AB specimens. However, the displacement at failure is significantly larger, reaching >8 mm, whereas it is close to 2 mm for the AB and HT200. The trend of the HT300 is significantly different, with a smooth decrease of the force after the peak is reached (occurring with a displacement of about 4 mm) and a second increment of the peak force. This second peak does not correspond to the densification phase, since the force decreases again, as can be observed for the HT300–1 specimen. This trend, with an oscillation of the force signal around a high mean force value, close to 7.5 kN, after the peak has been reached, is typical for structures used in high-absorbing applications, and allows for maximising the absorbed energy. Similar considerations can be drawn for the 3 × 3 × 3 specimens, with the AB and the HT200 showing similar trends and the HT300 specimens being characterized by a significantly larger displacement at failure. For these 3 × 3 × 3 specimens, the difference in peak stress between the HT200 and the AB specimens is larger with respect to that found for the 2 × 2 × 2 specimens (equal to about 11%), and the AB specimens show a larger displacement at failure. On the other hand, the trend of the force after the peak force is almost flat for the HT 300 specimens and this ensures higher energy absorption capabilities. It must be noted, moreover, that, for the same condition, the force displacement curves are very close and show small differences, with thus a limited experimental variability.

In order to investigate the influence of the number of cells on the compressive response, the stress-strain curves are compared in Fig. 8. The stress was computed assuming a fully solid cross-section, without accounting for the void space inherent to the lattice geometry, whereas the strain is computed as the displacement measured by the testing machine divided by the initial specimen length. For the quasi-static tests, all force–displacement curves are reported and discussed in the manuscript. For the stress–strain comparison in Fig. 8, only one representative curve for each condition is shown for the sake of clarity, since the corresponding repetitions exhibited only limited differences in peak stress and deformation trend.

According to Fig. 8, the size effect related to the number of cells has an overall limited influence on the compressive properties of the investigated lattice structures. Indeed, under the same testing conditions, the trend of the curve is very close, with limited differences in the peak stress, regardless of the specimen size and the number of cells under test. Therefore, it can be concluded that, at the specimen scale, the

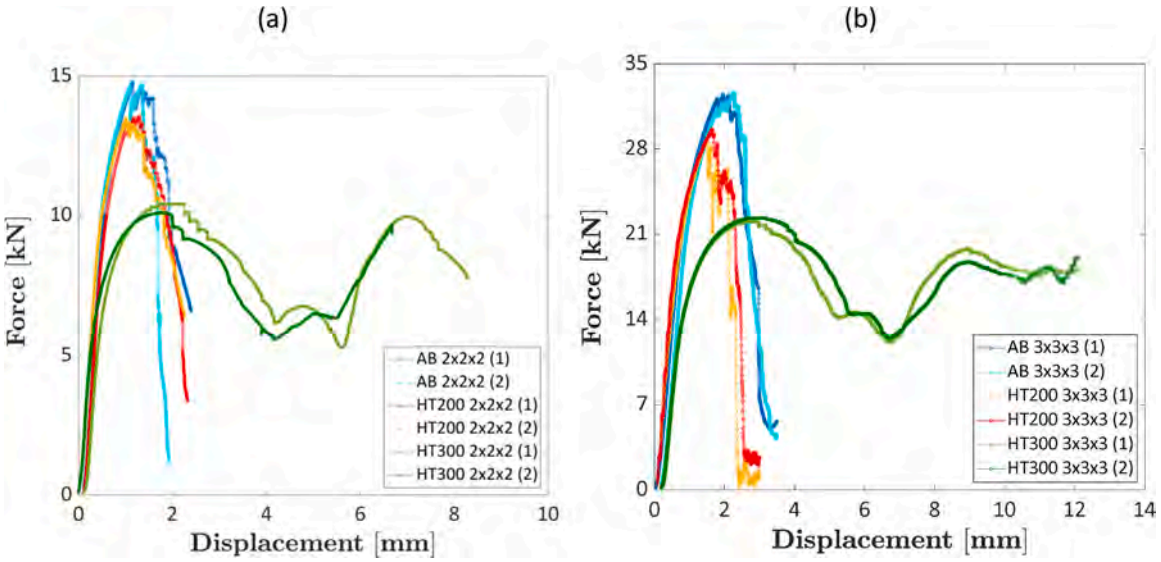

Fig. 7. Force-displacement curves from quasi-static compression tests for (a) 2 × 2 × 2 and (b) 3 × 3 × 3 lattice specimens in the AB, HT-200, and HT-300 conditions. The AB and HT-200 specimens show early peak load followed by abrupt force drop, whereas HT-300 exhibits a lower peak force and a more extended, stable crushing response, consistent with higher energy absorption.

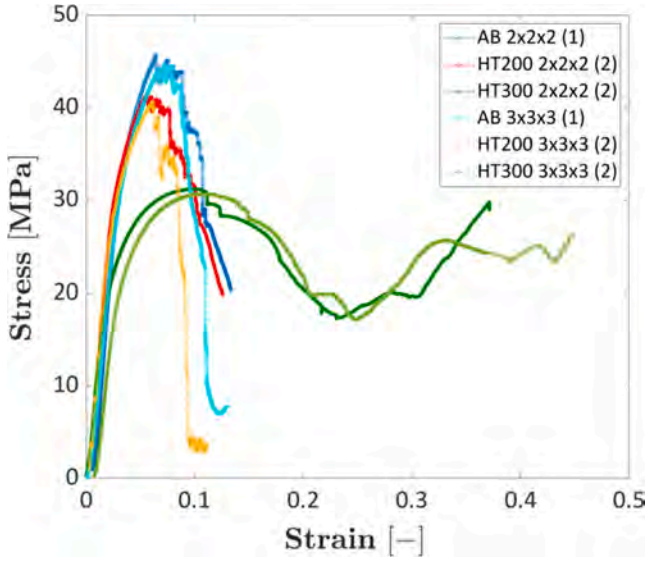

Fig. 8. Representative engineering stress-strain curves from quasi-static compression tests for 2 × 2 × 2 and 3 × 3 × 3 lattice specimens in the AB, HT-200, and HT-300 conditions. The curves are shown to compare the influence of specimen size and heat treatment on compressive response. For a given material condition, the two specimen sizes show similar trends, indicating a limited size effect within the investigated range.

number of cells has a limited, or negligible, influence on the energy absorption capability of the investigated lattice structures, regardless of the heat treatment and base material characteristics. At the same time, we explicitly acknowledge that extrapolation of these findings to larger structures should be further verified experimentally at the component scale.

Table 4 summarizes the main features concerning the compressive tests. In particular, the peak stress and the absorbed energy are reported. In the last column, Specific Absorbed Energy (SEA) is reported. The SEA is computed as the absorbed energy before densification divided by the specimen volume. Accordingly, the influence of the specimen size on the absorbing capabilities can be verified, since the SEA value is independent of the specimen volume. The average value of the two experimental tests is reported.

Table 4
Summary of the quasi-static compression results for the investigated lattice specimens. Reported quantities include average peak force, average peak stress, absorbed energy before densification, and specific absorbed energy (SEA). The values are averages of the two repetitions for each condition.

Specimen condition	Number of cells	Average peak force [N]	Average peak stress [MPa]	Average absorbed energy [J]	Average SEA [mJ/mm3]
AB	2 × 2 × 2	14,738	45	21.5	11.9
HT 200	2 × 2 × 2	13,537	42	21.6	11.4
HT 300	2 × 2 × 2	10,249	32	58.9	32.7
AB	3 × 3 × 3	32,550	45	68.4	11.8
HT 200	3 × 3 × 3	29,100	40	50.2	9.1
HT 300	3 × 3 × 3	22,150	30	206.5	35.6

According to Table 4, as expected, the absorbed energy is significantly larger after the HT300 heat treatment, being about 2 times and 4 times greater than that absorbed by the AB and HT200 specimens for the 2 × 2 × 2 and 3 × 3 × 3 configurations, respectively. For the 2 × 2 × 2 specimens, the SEA is almost equal in AB and HT 200 specimens and significantly larger for the HT 300 lattice structure specimens. For the 3 × 3 × 3 specimens, the SEA is slightly smaller for the AB specimen (with respect to the 2 × 2 × 2 specimens), whereas it is significantly smaller for the HT 200 specimens, passing from 11.4 mJ/mm3 for the 2 × 2 × 2 specimen to 9.1 mJ/mm3 for the 3 × 3 × 3 specimen. The lattice structure specimens subjected to the HT200 are therefore more prone to size effect, with the increment of the number of cells inducing a reduction of the specific absorbing capability and with defects contributing to a rapid decrease of the peak force, limiting the energy which can be absorbed, as can be seen in Fig. 7a and b. The SEA for the HT300 specimen is not affected by size-effect and, on the other hand, is larger for the 3 × 3 × 3 specimens. The HT300 allows not only an enhancement of the energy absorption capability, but also makes the material less sensitive to size effect and to the detrimental influence of defects, which, in a probabilistic framework, tends to increase their size with the increment of the material volume.

In Table 5, the peak-to-mean force ratio and crush efficiency are reported for the HT 300 specimens. These parameters could not be evaluated for the other sample configurations, since they exhibited abrupt failure, with a rapid drop in force after the peak load.

Table 5
Mean crushing force, peak-to-mean force ratio, and crush efficiency for the HT-300 specimens under impact loading. These crashworthiness indicators are reported only for HT-300 because this condition exhibited a sufficiently stable progressive crushing response.

Specimen condition	Impact speed [m/s]	Mean crushing force [N]	Peak to mean force ratio	Crush efficiency
HT 300	4	15,514	1.875	0.534
HT 300	8	17,211	1.865	0.536

In order to fully characterize the effect of the investigated heat treatments, the failure modes and the damage mechanisms have been compared. Fig. 9 shows the damage evolution for the 2 × 2 × 2 specimens, Fig. 9a for the AB specimen, Fig. 9b for the HT200 specimens and Fig. 9c for the HT300 specimens.

According to Fig. 9, the heat treatment significantly affects the damage evolution and the failure mechanisms and is the reason for the different absorption capability of the investigated specimens. In particular, for the AB and the HT200 specimens, the failure mode is quite similar. Indeed, beams randomly distributed within the specimens begin to fail, with a subsequent damage progression and the following failure of the joint between different beams. The initial failure is randomly distributed and occurs where the weakest site, for example a large internal or surface defect, is present. On the other hand, the HT300 specimen shows a completely different failure mode. Indeed, when the load is applied, almost all beams start deforming. This damage mechanisms progress as the applied load increases, but without a complete failure of the beams or of the node. In particular, the beams fold in on themselves smoothly. This explains why the force-displacement trend do not show an abrupt decrease of the force which remains almost flat after the peak force is reached, allowing to absorb a significantly larger amount of energy. As the damage progresses, the lower cells tend to compact reaching the maximum deformation before the densification phase and the test arrest. Even in this condition and when the maximum deformation is reached, the visible beams do not show complete failure, thanks to the high ductility induced by the HT300 and observed in the quasi-static tensile tests.

3.3.2. *Impact tests*

Impact tests have been carried out to verify the influence of load speed on the compressive response of the investigated specimen, also to verify if the possible strain rate effect is dependent and varies with the investigated heat treatments. Fig. 10 shows the result of the impact tests: Fig. 10a, c and e show the experimental Force displacement curves (two tests at 4 m/s and two tests at 8 m/s) for the AB, HT200 and HT300 specimens, respectively. Fig. 10b (for the AB specimens), d (for the HT200 specimens) and f (for the HT300 specimens) compare, for the same heat treatment, the force displacement curves for the quasi-static tests and impact tests at 4 m/s and 8 m/s. In these Figures, for the sake of clarity, one representative test for each condition is shown. Fig. 10g and h compares (one representative test for each condition) the impact tests at 4 m/s and 8 m/s.

According to Fig. 10a, for the AB specimens, the tests carried out at 4 m/s and 8 m/s show a similar trend, with no evident difference. Moreover, for the same impact speed, the two tests are very close, exhibiting a highly repeatable behaviour. Similar conclusions can be made for the HT200 specimen (Fig. 10c), with no evident strain rate effect by analysing the tests at 4 m/s and 8 m/s. However, for these specimens, the curves obtained at the same impact speed show some small differences, with different trends and peak forces. This difference can be related to a more pronounced sensitivity to defects and material irregularities, which can induce random local failures which influence and modify the resulting force-displacement curve. For the HT300 specimens (Fig. 10e), the force-displacement curves are similar, with the impact tests at 4 m/s achieving a smaller maximum displacement, as if the 8 m/s specimens can reach a more pronounced compaction. All specimens show an oscillating trend after the peak force is reached, regardless of the impact speed. The final displacement is larger for the 8 m/s impact, as a better and more efficient compaction can be obtained as the impact speed increases.

By comparing the tests carried out at 4 m/s and 8 m/s with the quasi-static test curve (Fig. 10b, d and f), the strain rate effect is, on the other hand, evident. The peak stress tends to increase, regardless of the specimen condition, as well as the displacement at failure. This can be attributed to a possible strain rate dependent behaviour of the AlSi10Mg

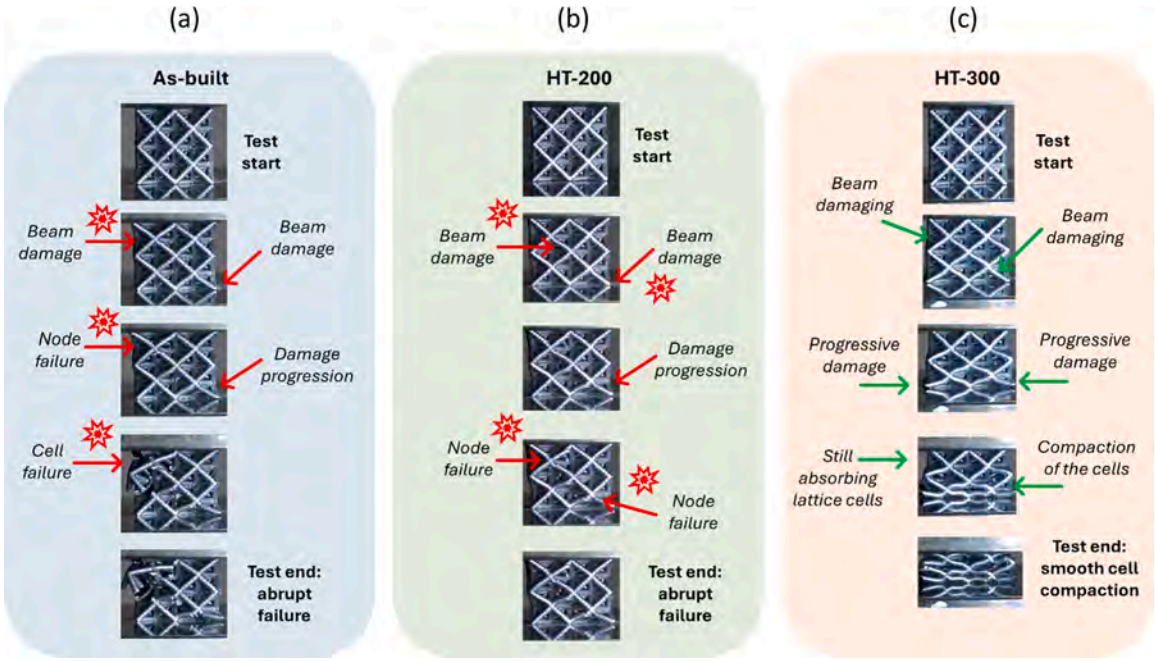

Fig. 9. Damage evolution during quasi-static compression of 2 × 2 × 2 lattice specimens: (a) AB, (b) HT-200, and (c) HT-300. The AB and HT-200 conditions show localized fracture and progressive joint failure, whereas HT-300 exhibits a more distributed deformation mode with progressive strut bending/folding and delayed rupture.

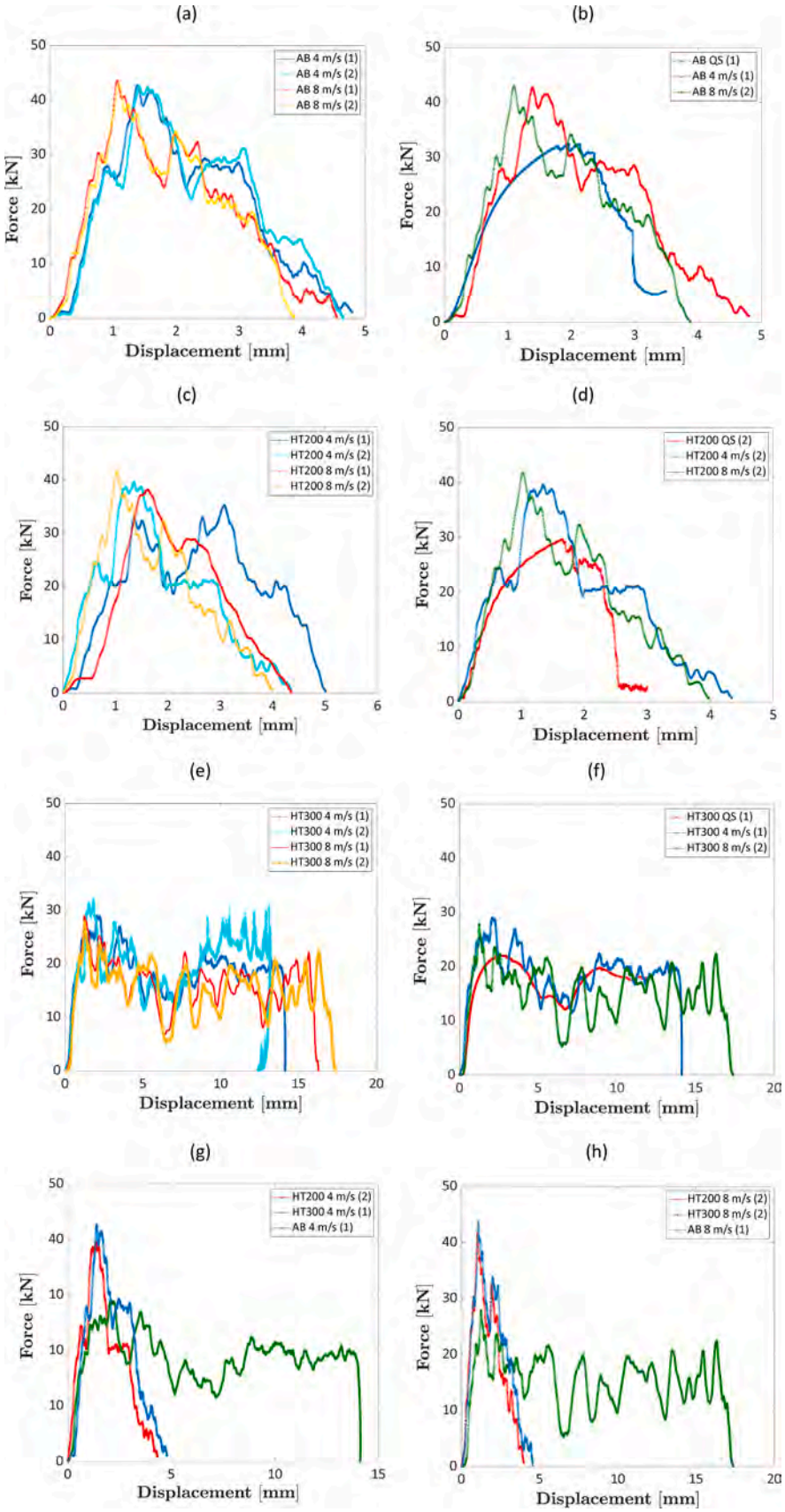

Fig. 10. Force-displacement curves from impact and quasi-static compression tests. Panels (a), (c), and (e) compare the two repetitions at 4 m/s and 8 m/s for the AB, HT-200, and HT-300 conditions, respectively. Panels (b), (d), and (f) compare representative quasi-static and dynamic curves for the same three conditions. Panels (g) and (h) compare the three material conditions at 4 m/s and 8 m/s, respectively. The results show a clear increase in peak force from quasi-static to dynamic loading, whereas the difference between 4 m/s and 8 m/s is limited within the investigated velocity range.

material under impact loads [77]. For the HT300 specimens, the trend is almost flat after the peak stress, but in the tests carried out at 4 m/s and 8 m/s, large oscillations can be observed, and this is a clear effect of increasing the impact speed and possible vibrations arising during the impact. Indeed, this effect is more evident for the largest tested impact speed, corresponding to 8 m/s. The effect of the heat treatment for the same impact speed is compared in Figs. 10 (Fig. 10*g* for 4 m/s and 10 h for 8 m/s). These Figures confirm the results of the quasi-static tests, with the HT 300 specimens characterized by a smaller peak force, but a significantly larger displacement at failure. The above commented force-displacement trends can be compared and investigated also by considering the failure modes and the damage evolution during the impact tests and recorded with the high-speed camera, shown in Fig. 11 for an impact speed of 4 m/s and 8 m/s.

According to Fig. 11, the damage mode of the AB and the HT200 specimens is very similar and close to that observed in the quasi-static tests. In particular, the damage process starts randomly, with subsequent beam failures. As the impactor continues to move down, the damage progressively expands as all cells collapse, with a rapid decrement after the peak stress is reached. For the HT300, the damage mode is the same found for the quasi-static test, regardless of the impact speed. Indeed, the beams start deforming when the impactor hit the specimen surface and these beams are subject to large deformation, allowing to absorb large quantities of energy. Even for these dynamic loads, the beams do not fail and do not break and gradually collapse and compact as the impact speed moves down.

Table 6 compares the peak force and the absorbed energy during the quasi-static and the impact tests. In order to better visualise the results, the peak forces and the absorbed energies are plotted with respect to the impact speed in Fig. 12a and Fig. 12b.

According to Table 6 and Fig. 12a, the peak force tends to increase from the quasi-static and dynamic tests. On the other hand, it remains quite constant for the investigated impact speed range, with the variation which can be ascribed to the experimental variability. This behaviour does not depend on the impact speed. Moreover, the peak force for the AB specimens shows, regardless of the testing condition. The absorbed energy, E_a, shows a similar trend. Indeed, E_a is the smallest for the quasi-static tests, and increases at an impact speed of 4 m/s and 8 m/s. The difference between E_a at 4 m/s and 8 m/s is limited, with an almost flat trend. The variability of the E_a values is smaller than the variability of the peak force, with the E_a of the two repetitions in the same testing conditions being very close. Since two repetitions were available for each configuration, the experimental scatter is discussed here mainly through the box plots reported in Fig. 12, rather than through standard-deviation-based metrics. Overall, the spread of the results remains limited, which is consistent with the micro-CT observations showing no major systematic differences among nominally identical specimens. The variability of peak force is more evident for the HT-200 condition, particularly under impact loading, whereas the variability of absorbed energy is smaller and becomes particularly limited for HT-300. This behaviour suggests that in the AB and HT-200 states the response is still strongly influenced by the random position of the most critical defect, which can trigger premature local failure, whereas in the HT-300 condition the more distributed crushing mode reduces the influence of individual critical defects on the overall energy absorption. The increase in absorbed energy can be attributed to the portion of energy absorbed due to the higher peak stress. In addition, a more uniform distribution of the damage evolution due to the dynamic load propagation can be the also be responsible for the higher absorbed energy, as well as inertial effects due to the impact speed. On the other hand, these factors have a negligible effect when the impact speed is increased from 4 m/s to 8 m/s, highlighting that the main influence is associated with the transition from quasi-static to dynamic loading. In contrast, within the dynamic domain, these effects remain almost unchanged even when the impact speed is doubled (within the investigated low-speed impact range).

4. Discussion

This section discusses the experimental results from a mechanistic standpoint to clarify how low-temperature heat treatment modifies the process-structure-property relationship of LPBF AlSi10Mg octet-truss lattices. The discussion first links the observed microstructural evolution to the measured changes in ductility, then interprets the corresponding deformation modes, failure initiation, and damage evolution under quasi-static and impact loading. Finally, the implications of the adopted octet-truss topology for crash-oriented design are discussed.

4.1. Heat treatment, microstructure and ductility

The experimental results indicate that the main effect of heat treatment is not simply a change in the nominal strength level of the alloy, but a progressive modification of the local deformation capacity available within the struts. This point is important because the crushing response of the lattice is governed not only by topology, but also by how much local plasticity can develop before fracture starts in the load-bearing members. The tensile results already show that the HT-200 condition remains relatively close to the AB state, whereas HT-300 produces a much larger strain to failure, despite the expected reduction in strength associated with the more evolved microstructure (Table 1).

The microstructural observations are consistent with this change in behaviour. In the lower-temperature condition, the microstructure is only partially altered, so the material retains a relatively limited local ductility. By contrast, after treatment at 300 °C, the Si-rich network becomes more fragmented and rounded, and the alloy enters a more ductile over-aged condition. This promotes a more homogeneous plastic flow and delays the nucleation of microcracks, which is particularly relevant in 3D printed lattice structures where stress concentrations are amplified by geometric imperfections and by the presence of internal defects.

From this perspective, heat treatment changes the way the lattice accommodates deformation before collapsing. In the AB and HT-200 conditions, the available local ductility is limited, so damage is more likely to start early at critical locations and propagate in a localized way. In the HT-300 condition, instead, the larger strain to failure allows the struts to deform more extensively before rupture, which changes not only the onset of damage, but also the overall sequence of crushing events.

4.2. Failure initiation, damage evolution and collapse mechanism

Under quasi-static loading, the difference between the three conditions is not limited to the magnitude of force and absorbed energy; it also concerns the way collapse develops. In the AB and HT-200 specimens, the crushing process remains predominantly fracture-dominated. Damage appears to initiate at isolated weak locations, most likely at defect-sensitive struts or at nodes where geometrical deviations and local stress concentrations are more severe. Once a small number of critical members fail, the load is redistributed only to a limited extent, and collapse proceeds through localized strut fracture followed by progressive node/joint failure. This interpretation is consistent with the abrupt drop observed after the first peak (Fig. 7a and b) and with the images showing broken members and damaged joints during compression (Fig. 9a and b).

The HT-300 condition behaves differently. Here, the collapse becomes noticeably more distributed, and the deformation is sustained by a larger number of struts over a longer portion of the crushing process. The images suggest that these members can undergo substantial axial yielding and bending, together with local plastic hinging or folding, before complete rupture occurs. This delays the onset of catastrophic failure and reduces the tendency of the structure to collapse through a single dominant fracture event. The nodes also remain intact for a longer

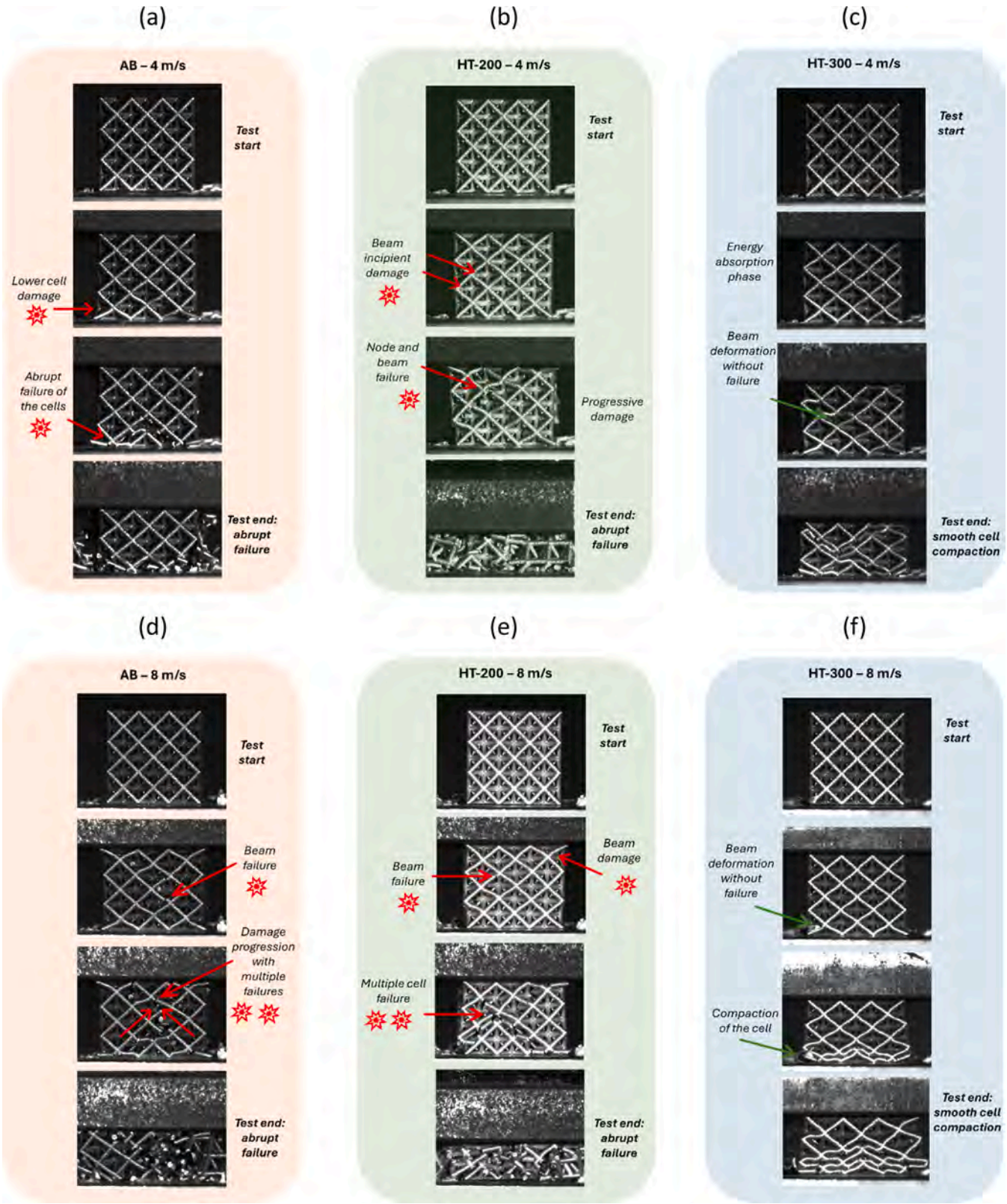

Fig. 11. Collapse sequence observed during impact tests for the three material conditions. Panels (a)–(c) correspond to 4 m/s and panels (d)–(f) to 8 m/s, for AB, HT-200, and HT-300, respectively. AB and HT-200 fail through localized rupture of struts and joints, whereas HT-300 shows a more progressive and ductile compaction mode with larger deformation prior to failure. The overall collapse mechanism remains qualitatively similar at 4 m/s and 8 m/s.

Table 6
Summary of the mechanical response measured in quasi-static and impact tests for the investigated lattice specimens. For each test, the table reports impact mass (when applicable), impact velocity, peak force, and absorbed energy.

Specimen	Impact mass [kg]	Impact speed [m/s]	Peak force [N]	Absorbed energy [J]
AB 1	30.98	4.099	42,704	94.59
AB 2	30.98	4.099	42,567	97.76
AB 3	7.982	8.102	43,552	89.90
AB 4	7.982	8.118	42,940	84.31
AB 1 QS	-	-	32,500	69.91
AB 2 QS	-	-	32,600	66.80
HT300 1	30.98	4.099	29,081	264.67
HT300 2	30.98	4.100	32,091	264.46
HT300 3	7.98	8.118	28,938	261.36
HT300 4	7.98	8.150	27,859	262.45
HT300 1 QS	-	-	22,000	205.85
HT300 2 QS	-	-	22,300	207.23
HT200 1	30.98	4.099	35,291	99.29
HT200 2	30.98	4.097	39,585	79.55
HT200 3	7.98	8.092	38,163	76.29
HT200 4	7.98	8.119	41,676	75.86
HT200 1 QS	-	-	28,600	46.86
HT200 2 QS	-	-	29,600	53.61

part of the loading history, which allows a more progressive load redistribution among adjacent cells. This is reflected in the smoother force-displacement response, the less pronounced post-peak drop, and the higher absorbed energy measured for HT-300 (Fig. 7a and b).

A similar ranking of mechanisms is observed under impact loading. The AB and HT-200 conditions still show a response governed by local rupture events, even though the absolute force level increases with loading rate. Damage continues to develop from a limited number of critical members and then propagates through neighboring struts and nodes, which indicates that the response remains sensitive to local weakness and fracture initiation. By contrast, the HT-300 specimens preserve a more distributed collapse mode even under dynamic conditions: the struts experience larger deformation before failure, lower cells compact progressively, and no abrupt member breakage comparable to the AB and HT-200 cases is evident in the visible collapse sequence (Fig. 11). The role of HT-300 can therefore be interpreted as a shift from a defect-sensitive and fracture-dominated response to a more ductile plastic-collapse regime, and this shift remains visible in both quasi-static and impact tests.

For clarity, the main features of the observed collapse mechanism are summarized in Table 7.

This interpretation is also consistent with the observed experimental scatter. When collapse is governed by early localized fracture, as in the AB and HT-200 conditions, the response is more sensitive to the location and severity of the most critical defect, which may cause larger specimen-to-specimen differences in peak force. By contrast, the more distributed crushing mode observed in HT-300 makes the global response less dependent on a single critical flaw and therefore leads to a more stable absorbed-energy response, which is particularly relevant for crash applications where repeatability is as important as peak performance.

4.3. Topology choice and implications for crash oriented design

The present results should also be interpreted in light of the adopted octet-truss topology. As a stretch-dominated architecture, the octet-truss is attractive for lightweight applications where relatively high stiffness and efficient load transfer are required. At the same time, it is important to recognize that bending-dominated lattices often exhibit longer and more stable crushing plateaus and may achieve higher specific energy absorption at comparable relative density. For this reason, the present study does not aim to claim that the octet-truss is the universally optimal topology for crash absorption. Rather, it uses a canonical and mechanically well-understood lattice to isolate the effect of heat treatment from the additional variables introduced by topology changes. In this sense, the octet-truss serves as a useful reference architecture for studying whether a geometry-free design variable, such as heat treatment, can significantly alter crash response.

This choice also helps frame the practical significance of the results. In a stretch-dominated lattice, unstable collapse or premature member fracture can compromise the expected load-bearing efficiency. The fact that HT-300 promotes a more progressive and distributed crushing mode is therefore especially relevant, because it shows that the intrinsic limitations of a conventional octet-truss can be partially mitigated without redesigning the unit cell. In other words, the treatment does not change the lattice topology, but it changes how that topology is

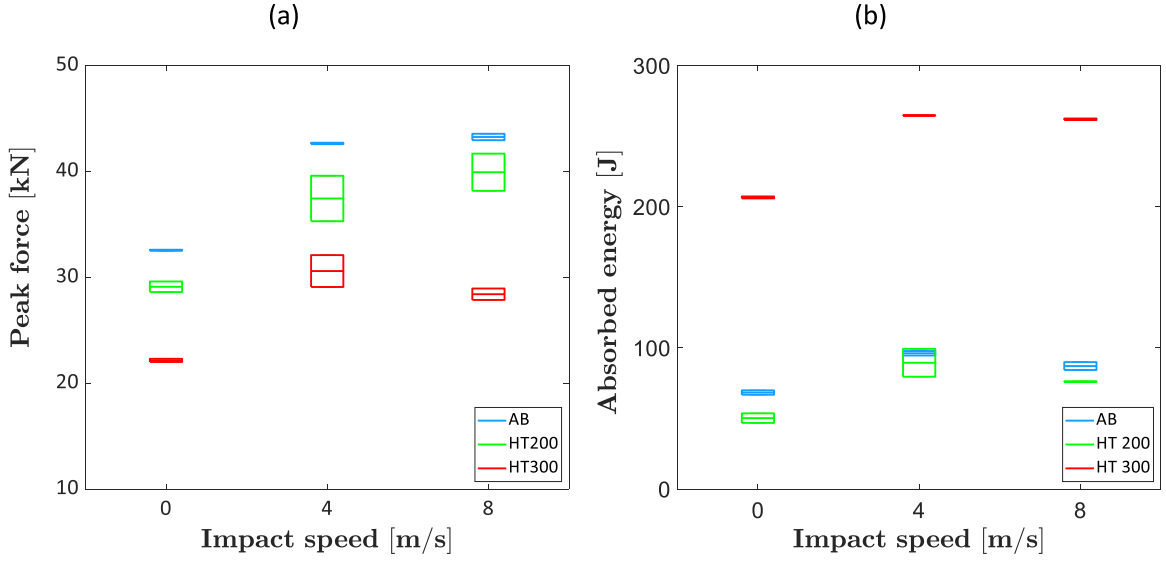

Fig. 12. Variation of (a) peak force and (b) absorbed energy with loading speed for the AB, HT-200, and HT-300 conditions. For all materials, peak force increases from quasi-static to dynamic loading, while the difference between 4 m/s and 8 m/s remains limited. HT-300 consistently provides the highest absorbed energy, confirming the beneficial effect of the 300 °C heat treatment on crash performance.

Table 7
Summary of the microstructure-dependent collapse mechanisms observed in the investigated lattice conditions, including qualitative information on microstructural state, failure initiation, collapse mode, and macroscopic crushing response.

Configuration	Microstructural state	Failure initiation	Collapse mode	Macroscopic response
As built	Limited ductility	Early initiation	Localized structure fracture	Abrupt post peak drop, unstable crushing
HT 200	Limited ductility	Early initiation	Localized structure fracture	Abrupt post peak drop, unstable crushing
HT 300	More evolved and ductile state	Delayed and more distributed initiation	Axial yielding/ bending, local plastic folding.	Smoother plateau-like response, progressive compaction, higher absorbed energy

activated during crushing.

From a crash-design perspective, this has a direct implication. A response governed by localized fracture and early node failure tends to produce less stable collapse and more abrupt force variations, whereas a more distributed plastic-collapse mode favours smoother compaction and more predictable energy dissipation. This is precisely the type of behaviour that becomes valuable when the lattice is transferred from specimen scale to a component-level absorber. The more stable crushing response measured for HT-300 therefore provides the physical basis for the design strategy developed in the following section, where the thermally tuned lattice is used to build an automotive crash absorber under prescribed energy and packaging constraints. At the same time, the present conclusions should be interpreted within the limits of the investigated octet-truss architecture, and further work is needed to assess whether the same thermal-tuning strategy yields comparable or even stronger benefits in bending-dominated or TPMS-based lattices.

5. Design of a crash absorber by finite element modelling

This section moves from specimen-scale interpretation to component-scale design. First, the finite element model is introduced and validated against the quasi-static and impact experiments in the HT-300 condition. The validated model is then used to design and assess a lattice-based automotive crash absorber under realistic energy and packaging constraints.

5.1. FE model of the compression tests

The lattice structures are modelled with 1D beam elements, which are able to well capture the compressive response without affecting the computational efficiency, as in the case of 3D solid elements [78]. The struts have been discretized with 1.0 mm long Hughes-Liu beam elements, as determined through a convergence analysis.

Material behaviour is modelled with an elasto-plastic law, whose plastic regime is that identified through tensile tests on specimen heat-treated at 300 °C (cf. Table 1). The strain rate sensitivity is modelled with the Cowper-Symonds model, whose material characteristics C and p are determined with a trail-and-error process by comparison with the experimental results of the dynamic test at 4 m/s. The impact test at 8 m/s is instead used for validation.

The compression tests have been replicated by means of two rigid walls disposed above and below the specimen, one fixed and one moving with a prescribed motion law. More in detail, in the case of the quasi-static tests, the rigid wall moves with constant speed, as in the experimental test. In the dynamic impact tests, the rigid wall has an initial kinetic energy, with mass and initial velocity defined in accordance with the simulated test.

5.2. Validation of the FE model

Figs. 13 compare the experimental and numerical results of the quasi-static tests. Fig. 13a reports the comparison of the 2 × 2 lattice specimen, while Fig. 13b shows the results of the 3 × 3 structure.

According to Figs. 13, the model well replicates the global behaviour of the lattice structure, with the force oscillating as result of the progressive crushing. The resulting force-displacement curve slightly overestimates the experimental trend. The estimated peak force and the mean crushing force are on average 13% and 25% higher than the experimental results, respectively. This can be attributed to the presence of internal defects, which have been shown to affect the crushing performance of lattice structures [28,79]. Both the 2 × 2 and the 3 × 3 models well capture the progressiveness of the crushing phenomenon, as highlighted in Figs. 13.

Fig. 14a and Fig. 14b show the results of the 4 m/s impact and 8 m/s impact, respectively.

The C and p parameters of the Cowper-Symonds model have been found equal to 6500 and 1.25, respectively, by comparison with the results of the impact test at 4 m/s, and validated on the results of the impact test at 8 m/s. Oscillations observed in the experimental results are mainly caused by inertial effects combined with the position of the load cell. The load, positioned at the top of the impactor, indeed acquired its longitudinal vibrations as result of the impact event. Nevertheless, the numerical model well captures the average force-intrusion curves, as well as the progressive crushing behaviour of the structure. The estimated mean crushing force is on average 10% higher than that obtained in the experimental test.

The agreement between the experimental and numerical data validates the numerical model, which can be reliably adopted in the design of an automotive crash absorber made of octet strut lattice structures.

5.3. Automotive crash absorber made of octet strut lattice structures

Crash absorbers must dissipate the kinetic energy of the vehicle in low-speed accident events, that is 15 km/h according to the RCAR structural crash protocol, to protect passengers and reduce damage to other components, such as the radiator. In the worst-case scenario, that is the 40% overlap impact, a single crash absorber must dissipate the whole kinetic energy of the vehicle in the accident.

To assume a realistic design scenario, a C segment vehicle, namely a Toyota Yaris whose LS-Dyna model is available at [80], is retained, whose mass is 1400 kg. Accordingly, the energy to dissipate in an accident at 15 km/h is 12.1 kJ. Moreover, for replacing the crash absorber, envelope and mass constraints must be accounted for. The crash tube has a mass of 1.05 kg and dimensions 235 mm in length and 89×109 mm in the cross-section, with a wall thickness of 1.8 mm.

The crash absorber must be designed to avoid global buckling, thus guaranteeing a progressive crushing behavior, as well as the peak force must be limited, as it can induce critical deceleration for passengers.

Preliminary simulations on rectangular solid shaped crash absorbers have been performed to assess the influence of the cross-section dimensions and of the strut diameter on the mean crushing force and absorbed energy until densification. Each rectangular solid shaped crash absorber presents a square cross-section with repetitions of unit cells and has a length of 5 unit-cells, i.e., 42.5 mm, to avoid buckling. For example, the 4 × 4 crash absorber has 16 unit-cells in the cross-section. Strut diameter has been varied between 0.8 and 1.4 mm on the 8 × 8 crash absorber. Results of the preliminary simulations are reported in Figs. 15.

This analysis allows to identify preliminary dimensions of the crash absorber. For example, for a 5 × 5 unit-cells cross-section, which has a

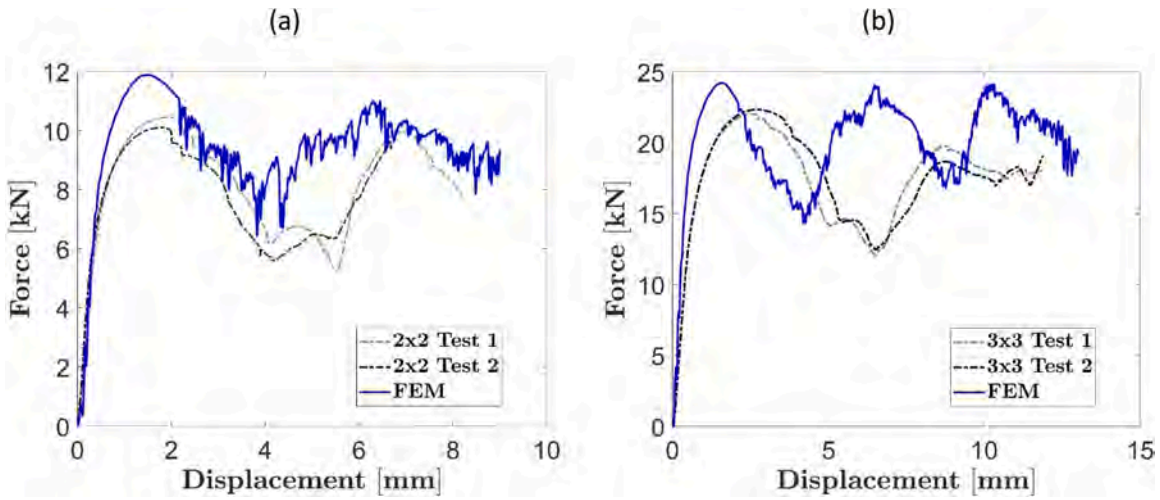

Fig. 13. Comparison between experimental and numerical force-displacement curves under quasi-static compression for HT-300 lattice specimens: (a) 2 × 2 × 2 and (b) 3 × 3 × 3. The FE model captures the global progressive crushing trend and the oscillatory response associated with successive collapse events, although it slightly overestimates the experimental force level.

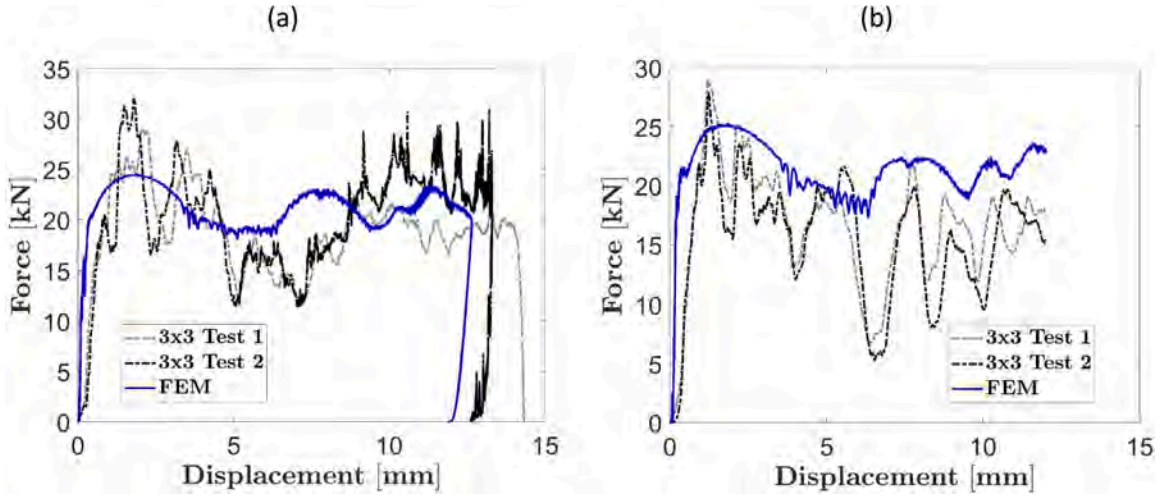

Fig. 14. Comparison of force-displacement curve under impact: a) 4 m/s impact velocity; b) 8 m/s impact velocity. The quasi static and dynamic models properly follow the experimental trend.

transversal envelope of 42.5 × 42.5 mm and absorbs almost 0.25 kJ per row of unit-cells, 50 unit-cells in length are required to absorb 12.1 kJ. However, rather than progressively crushing, a crash absorber of 5 × 5 × 50 unit-cells presents undesired global buckling, which strongly limits the energy absorption capability of the structure. Similar behavior has been observed with a 6 × 6 × 35 crash absorber. On the contrary, in a 7 × 7 × 25 or in an 8 × 8 × 20 absorbers, given the high mean crushing force, high deceleration is obtained from the beginning of the intrusion event, which can be critical for passengers. This effect can be mitigated by reducing the strut diameter, as shown in Fig. 15c.

Accordingly, to limit the deceleration, while avoiding global buckling, the automotive crash absorber has been designed with a variable strut diameter along its length. A linear variation between 0.8 and 1.4 mm has been retained from the top to the bottom of the component. Fig. 16a shows the crash absorber with variable strut diameter, which is made of 8 × 8 × 25 unit cells, i.e., the cross-section envelope is 68×68 mm and the length is 212.5 mm, in accordance with the envelope constraints of the retained vehicle.

The different colors of Fig. 16a highlight the different strut diameters of each row of unit cells. Figs. 16b and 16 c compare the force-intrusion response and the acceleration profiles of the proposed crash absorber and of the crash tube equipping the vehicle, respectively.

As shown, in the crash absorber made of octet truss lattice structures, the force linearly increases and slightly oscillates, as result of the linear variation of the strut diameter. Moreover, in comparison with the standard crash tube, the lattice absorber prevents the occurrence of peak deceleration values, in favor of the occupants' safety. This is due to the progressive crushing behavior of the lattice-based structure, as shown in Fig. 16d Although both solutions satisfy the required crash-energy target, the proposed lattice absorber achieves a substantially higher mass efficiency, with the SEA increasing from 11.5 kJ/kg for the reference crash tube to 20.16 kJ/kg for the proposed design, corresponding to an improvement of about 67%. At the same time, the lattice-based solution provides a smoother force-intrusion response and lower peak deceleration, which are beneficial for crash-management applications.

In addition to the superior crashworthiness, the crash absorber made of lattice structures allows to reduce the total mass of the component to 0.6 kg, that represents >40% of reduction with respect to the standard crash tube. The global envelope is also reduced, being the cross-section envelope of the lattice absorber equal to 68×68 mm with length equal to 212.5 mm, which facilitates the housing of other components. According to the results of Figs. 16, the crash absorber with variable diameter

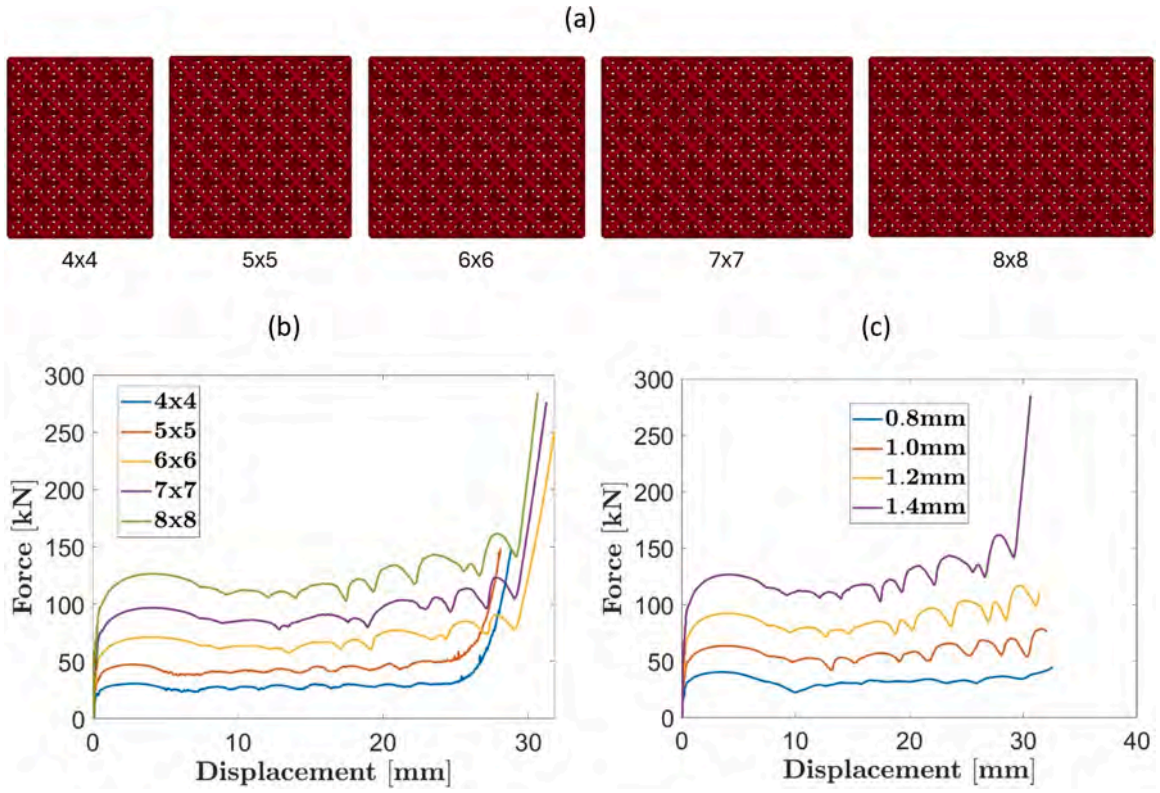

Fig. 15. Preliminary numerical analyses used to size the lattice-based automotive crash absorber: (a) example of the rectangular lattice absorber used in the parametric study, (b) influence of cross-section size on mean crushing force, and (c) influence of strut diameter for the $8 \times 8 \times 5$ configuration. Increasing the number of cells or the strut diameter increases the mean crushing force and modifies the absorber design space.

allows to achieve smooth force-intrusion behavior, while significantly reducing the mass component.

This analysis highlights that octet truss lattice structures, known for their strength, can be adopted in energy absorption applications by properly exploiting the process-structure relationship. The structural response can be tailored to energy absorption applications, such as the crash absorber of an automotive vehicle, achieving significant improvements in terms of crashworthiness, mass and global envelope reduction, with respect to the currently adopted crash tube.

6. Conclusions

This study investigated the process-structure-property relationship of LPBF AlSi10Mg octet-truss lattices for crash-absorption applications, with particular focus on the role of low-temperature heat treatment as a geometry-free design variable. The experimental results showed that heat treatment strongly affects the crushing response of the lattice, even though the unit-cell topology remains unchanged. In particular, the HT-300 condition provided the clearest improvement: compared with the as-built and HT-200 states, it reduced the force peak, increased the deformation before collapse, and significantly enhanced the specific energy absorption under both quasi-static (around 4 times higher) and low-velocity impact loading (around 3 times higher) . By contrast, HT-200 produced only limited benefits and remained mechanically closer to the as-built condition.

The observed macroscopic response is consistent with the microstructural evolution induced by thermal treatment. The EBSD analysis and tensile results indicate that HT-300 promotes a more ductile material state, associated with a more evolved Si-rich network and a markedly higher local strain-to-failure. This change in local deformation capacity alters the collapse mechanism of the lattice. In the as-built and HT-200 conditions, crushing remains dominated by early localized fracture and abrupt post-peak force drop, making the response more sensitive to critical defects. In HT-300, instead, the collapse becomes more distributed and progressive, with struts undergoing larger deformation before rupture and with a smoother plateau-like response. This shift from a defect-sensitive fracture-dominated regime to a more ductile plastic-collapse regime is the main physical reason for the improved crashworthiness.

From a design perspective, these results show that heat treatment can be used as an effective post-process lever to tailor the crash response of additively manufactured lattices without modifying the geometry. This concept was further confirmed at component level through FE-based design of a lattice crash absorber for automotive applications. The proposed HT-300-based solution satisfied the 12.1 kJ crash-energy target of a segment C vehicle while reducing the component mass by $>$40% compared with a conventional crash tube. At the same time, the component-level specific energy absorption increased from 11.5 kJ/kg for the reference crash tube to 20.16 kJ/kg for the proposed lattice absorber, corresponding to an improvement of about 67%, together with a smoother force-intrusion response and lower peak deceleration. These conclusions should nevertheless be interpreted within the limits of the investigated octet-truss architecture and relative-density range, but the proposed strategy is promising and flexible and is expected to potentially be applied to other geometry.

CRediT authorship contribution statement

Alessandro Benelli: Writing – review & editing, Writing – original draft, Visualization, Validation, Formal analysis, Data curation. **Carlo Boursier Niutta:** Writing – review & editing, Writing – original draft, Investigation, Data curation. **Andrea Tridello:** Writing – review & editing, Writing – original draft, Supervision, Project administration, Formal analysis, Conceptualization.

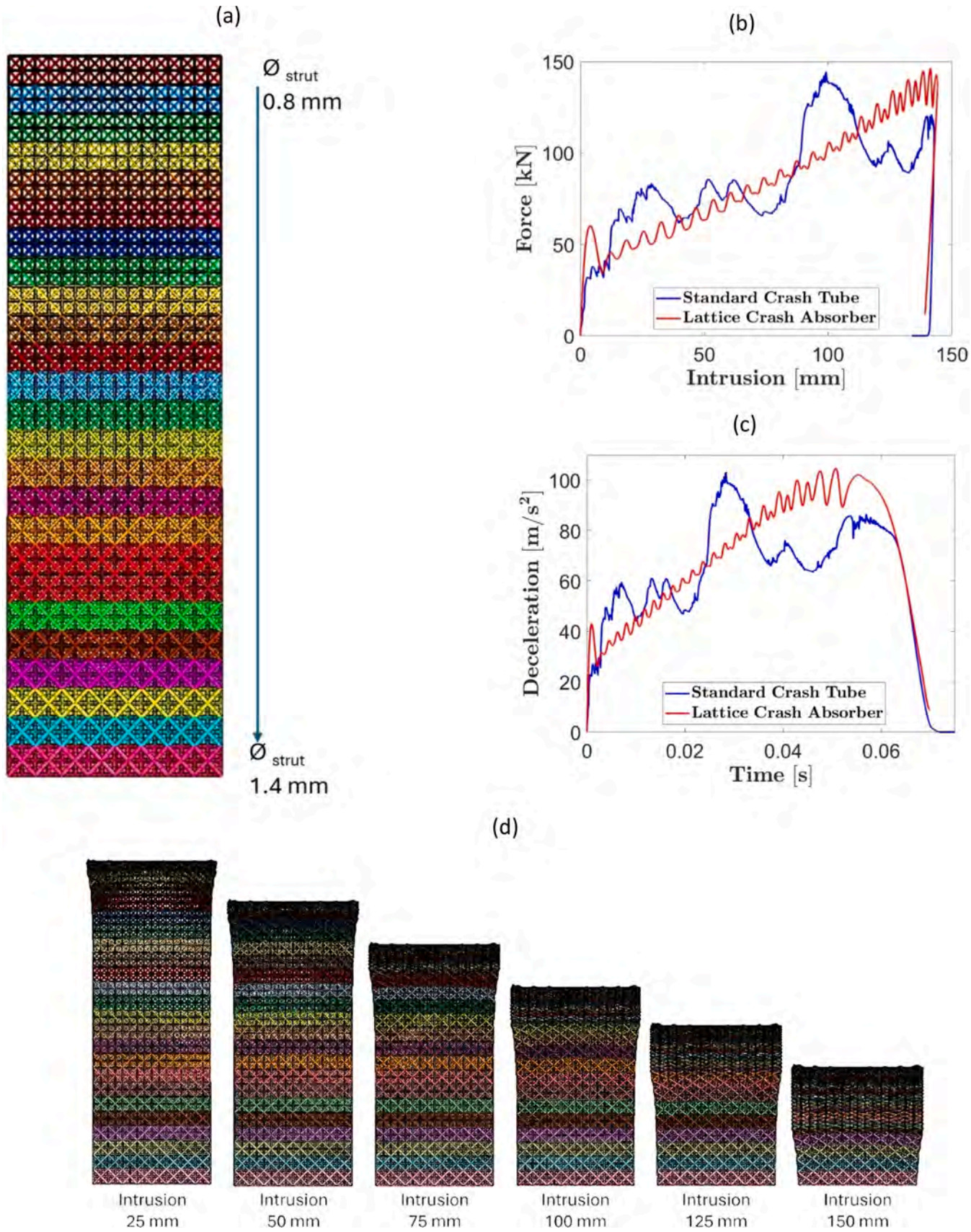

Fig. 16. Lattice-based automotive crash absorber designed with a linearly varying strut diameter: (a) geometry of the proposed absorber, (b) comparison of force-intrusion response with the reference crash tube, (c) comparison of deceleration histories, and (d) simulated crushing sequence of the lattice absorber. The graded lattice design provides progressive crushing, smoother force development, and lower peak deceleration while satisfying the crash-energy target.

Declaration of competing interest

The authors declare that they have no known competing financial interests or personal relationships that could have appeared to influence the work reported in this paper.

Data availability

Data will be made available on request.

References

[1] T. DebRoy et al., "Additive manufacturing of metallic components – process, structure and properties," 2018, *Elsevier Ltd.* doi:10.1016/j.pmatsci.2017.10.001.

[2] Zhou L, et al. Additive manufacturing: a comprehensive review. Multidiscip Digit Publ Inst May 01, 2024;24:2668. https://doi.org/10.3390/s24092668.

[3] Asapu S, Kumar YR. Design for Additive manufacturing (DfAM): a comprehensive review with case study insights. JOM 2025;77(5):3931–51. https://doi.org/10.1007/s11837-025-07164-x.

[4] K. Kanishka and B. Acherjee, "Revolutionizing manufacturing: a comprehensive overview of additive manufacturing processes, materials, developments, and challenges," 2023, *Elsevier Ltd.* doi:10.1016/j.jmapro.2023.10.024.

[5] Zhu J, Zhou H, Wang C, Zhou L, Yuan S, Zhang W. A review of topology optimization for additive manufacturing: status and challenges. Chin J Aeronaut 2021;34:91–110. https://doi.org/10.1016/j.cja.2020.09.020.

[6] J. Liu et al., "Current and future trends in topology optimization for additive manufacturing," 2018, *Springer Verlag.* doi:10.1007/s00158-018-1994-3.

[7] M. Bayat et al., "Holistic computational design within additive manufacturing through topology optimization combined with multiphysics multi-scale materials and process modelling," 2023, *Elsevier Ltd.* doi:10.1016/j.pmatsci.2023.101129.

[8] G.P. Borikar, A.R. Patil, and S.B. Kolekar, "Additively manufactured lattice structures and materials: present progress and future scope," 2023, *SpringerOpen.* doi:10.1007/s12541-023-00848-x.

[9] Gao C, et al. Mechanical properties and energy absorption capabilities of plate-based AlSi10Mg metamaterials produced by laser powder bed fusion. J Mater Res Technol 2024;30:3851–62. https://doi.org/10.1016/j.jmrt.2024.04.114.

[10] Noronha J, et al. Thin-plate lattices in AlSi10Mg alloy via laser additive manufacturing: highly enhanced specific strength and recovery. Addit Manuf 2025;99:104664. https://doi.org/10.1016/j.addma.2025.104664.

[11] Nammalvar Raja Rajan A, et al. Micromechanical modeling of AlSi10Mg processed by laser-based additive manufacturing: from as-built to heat-treated microstructures. Mater (Basel) Aug. 2022;15(16):5562. https://doi.org/10.3390/ma15165562.

[12] Sun LL, et al. Design and comparative numerical analysis of AlSi10Mg PBF-LB/M manufactured TPMS lattice structures for improved mechanical performance. Mater (Basel) Nov. 2025;18(21):4934. https://doi.org/10.3390/ma18214934.

[13] Khanna P, Sood S, Mishra P, Bharadwaj V, Aggarwal A, Singh SJ. Analysis of compression and energy absorption behaviour of SLM printed AlSi10Mg triply periodic minimal surface lattice structures. Structures 2024;64:106580. https://doi.org/10.1016/j.istruc.2024.106580.

[14] Zhang J, et al. Bidirectional-gradient TPMS for enhanced energy absorption performance: design, experiments, and simulation. Thin-Walled Struct 2026;220:114357. https://doi.org/10.1016/j.tws.2025.114357.

[15] Fayyaz, Bashmal S, Nazir A, Khan S, Alofi A. Damping optimization and energy absorption of mechanical metamaterials for enhanced vibration control applications: a critical review. Multidiscip Digit Publ Inst Jan. 01, 2025;17:237. https://doi.org/10.3390/polym17020237.

[16] Wang X, Wang S, Huang M, Qin R, Chen B. Multifunctional strut-plate composite lattice metamaterial for integrated acoustic, energy, and vibration management. Virtual Phys Prototyp 2025;20(1). https://doi.org/10.1080/17452759.2025.2499469.

[17] Jiang W, Yin G, Xie L, Yin M. Multifunctional 3D lattice metamaterials for vibration mitigation and energy absorption. Int J Mech Sci 2022;233:107678. https://doi.org/10.1016/j.ijmecsci.2022.107678.

[18] Yang J, Liu H, Cai G, Jin H. Additive manufacturing and influencing factors of lattice structures: a review. Multidiscip Digit Publ Inst (MDPI) Apr. 01, 2025;18:1397. https://doi.org/10.3390/ma18071397.

[19] Tao C, et al. Crashworthiness of additively manufactured lattice reinforced thin-walled tube hybrid structures. Aerospace Jun. 2023;10(6):524. https://doi.org/10.3390/aerospace10060524.

[20] Berthel J, Taggart-Scarff J, Yu J, McWilliams B, Panat R, Beuth J. AlSi10Mg plate-lattice structures fabricated by laser powder bed fusion exhibiting high specific energy absorption. Mater Des 2025;257:114395. https://doi.org/10.1016/j.matdes.2025.114395.

[21] Syrlybayev D, Yankin A, Perveen A, Talamona D. Effect of topology on the mechanical properties and energy absorption of annealed lightweight SLM AlSi10Mg lattice structures. Int J Lightweight Mater Manuf 2026;9:300–13. https://doi.org/10.1016/j.ijlmm.2025.10.005.

[22] AlQaydi HA, et al. Hybridisation of AlSi10Mg lattice structures for engineered mechanical performance. Addit Manuf 2022;57:102935. https://doi.org/10.1016/j.addma.2022.102935.

[23] Deshpande VS, Ashby MF, Fleck NA. Foam topology bending versus stretching dominated architectures. Online]. Available: www.elsevier.com/locate/actamat; 2001.

[24] Gregg CE, Kim JH, Cheung KC. Ultra-light and scalable composite lattice materials. Adv Eng Mater 2018;20(9). https://doi.org/10.1002/adem.201800213.

[25] W. Yan et al., "Modeling process-structure-property relationships for additive manufacturing," 2018, *Higher Education Press.* doi:10.1007/s11465-018-0505-y.

[26] Wang J, Panesar A. Machine learning based lattice generation method derived from topology optimisation. Addit Manuf 2022;60:103238. https://doi.org/10.1016/j.addma.2022.103238.

[27] Jia Z, Gong H, Liu S, Zhang J, Zhang Q. Designing three-dimensional lattice structures with anticipated properties through a deep learning method. Mater Des 2024;244:113139. https://doi.org/10.1016/j.matdes.2024.113139.

[28] Ciampaglia A, Boursier Niutta C, Benelli A, Tridello A. Compressive response of lattice structures: a multiscale approach to model the influence of internal defects. Prog Addit Manuf 2025;10(7):4107–21. https://doi.org/10.1007/s40964-025-01026-3.

[29] Liang X, et al. Inherent strain homogenization for fast residual deformation simulation of thin-walled lattice support structures built by laser powder bed fusion additive manufacturing. Addit Manuf 2020;32:101091. https://doi.org/10.1016/j.addma.2020.101091.

[30] Cibrario L, Gastaldi C, Delprete C, Cozza IF. Mechanical design of lattice metamaterials: a multiscale homogenization-based operational procedure. Mater Des 2025;251:113614. https://doi.org/10.1016/j.matdes.2025.113614.

[31] J. Somnic and B.W. Jo, "Status and challenges in homogenization methods for lattice materials," Jan. 01, 2022, *MDPI.* doi:10.3390/ma15020605.

[32] Luo T, Wang L, Liu F, Chen M, Li J. Modal response improvement of periodic lattice materials with a shear modulus-based FE homogenized model. Mater (Basel) Mar. 2024;17(6):1314. https://doi.org/10.3390/ma17061314.

[33] R. Wang et al., "Additive manufacturing of metal lattice structures: a comprehensive review of technologies, mechanical properties, applications, and future trends," 2025, *Elsevier Ltd.* doi:10.1016/j.mtphys.2025.101933.

[34] Li Y, Jiang D, Zhao R, Wang X, Wang L, Zhang LC. High mechanical performance of lattice structures fabricated by additive manufacturing. Multidiscip Digit Publ Inst Oct. 01, 2024;14:1165. https://doi.org/10.3390/met14101165.

[35] S.B. Akula, C. S.C., D.V. Seshagirirao, S. Suryakumar, A. Hafeezur Rahman, and N. S. Reddy, "Metallic lattice structures via additive manufacturing: applications, challenges and opportunities in aerospace and defence," 2026, *Elsevier Ltd.* doi:10.1016/j.jmapro.2025.12.045.

[36] Ding J, Qu S, Zhang L, Wang MY, Song X. Geometric deviation and compensation for thin-walled shell lattice structures fabricated by high precision laser powder bed fusion. Addit Manuf 2022;58:103061. https://doi.org/10.1016/j.addma.2022.103061.

[37] Zhang L, Lifton J, Hu Z, Hong R, Feih S. Influence of geometric defects on the compression behaviour of thin shell lattices fabricated by micro laser powder bed fusion. Addit Manuf 2022;58:103038. https://doi.org/10.1016/j.addma.2022.103038.

[38] Alghamdi A, Maconachie T, Downing D, Brandt M, Qian M, Leary M. Effect of additive manufactured lattice defects on mechanical properties: an automated method for the enhancement of lattice geometry. Int J Adv Manuf Technol 2020;108(3):957–71. https://doi.org/10.1007/s00170-020-05394-8.

[39] Amirian A, Battley M, Diegel O, Amirpour M. Additive manufacturing defects in polymeric lattice structures: a comprehensive analysis of morphology, distribution, and printing orientation influence. Int J Adv Manuf Technol 2025;140:5361–84. https://doi.org/10.1007/s00170-025-16521-8.

[40] Zhao C, Wang H, Li Z, Liu W, Bian H, Zhang K. Process optimization and anisotropic compression performance of AlSi10Mg BCC lattice fabricated by selective laser melting. Appl Phys Mater Sci Process 2025;131(8). https://doi.org/10.1007/s00339-025-08726-1.

[41] Salvi L, Smaniotto B, Hild F, Tarantino MG. Tensile deformation and failure of AlSi10Mg random cellular metamaterials. Int J Mech Sci 2024;281:109612. https://doi.org/10.1016/j.ijmecsci.2024.109612.

[42] Hu Y, She Y, Wu S, Kan Q, Yu H, Kang G. Critical physics-informed fatigue life prediction of laser 3D printed AlSi10Mg alloys with mass internal defects. Int J Mech Sci 2024;284:109730. https://doi.org/10.1016/j.ijmecsci.2024.109730.

[43] Zhang Y, et al. Simultaneous enhancement of mechanical and functional properties by heat-treatment in CuAlNi shape memory alloys fabricated by laser powder bed fusion. Addit Manuf 2024;84:104099. https://doi.org/10.1016/j.addma.2024.104099.

[44] Fiocchi J, Bregoli C, Gerosa G, Tuissi A, Biffi CA. Tuning of static and dynamic mechanical response of laser powder bed fused AlSi10Mg lattice structures through heat treatments. Adv Eng Mater 2021;23(10). https://doi.org/10.1002/adem.202100418.

[45] Noronha J, Leary M, Brandt M, Qian M. AlSi10Mg hollow-strut lattice metamaterials by laser powder bed fusion. Mater Adv Mar. 2024;5(9):3751–70. https://doi.org/10.1039/d3ma00813d.

[46] Disayanan D, Buntornvorapan P, Sukprasertchai T, Uthaisangsuk V. Improving energy absorption and failure characteristic of additively manufactured lattice structures using hollow and curving techniques. Compos Struct 2024;337:118067. https://doi.org/10.1016/j.compstruct.2024.118067.

[47] Xiao L, Feng G, Li S, Mu K, Qin Q, Song W. Mechanical characterization of additively-manufactured metallic lattice structures with hollow struts under static and dynamic loadings. Int J Impact Eng 2022;169:104333. https://doi.org/10.1016/j.ijimpeng.2022.104333.

[48] Zhao M, Li X, Zhang DZ, Zhai W. Design, mechanical properties and optimization of lattice structures with hollow prismatic struts. Int J Mech Sci 2023;238:107842. https://doi.org/10.1016/j.ijmecsci.2022.107842.
[49] Noronha J, et al. Engineering hollow-strut lattice nodes for enhanced load-bearing with cubic symmetry. Int J Mech Sci 2025;307:110923. https://doi.org/10.1016/j.ijmecsci.2025.110923.
[50] Adelmann B, Hellmann R. Mechanical properties of LPBF-built titanium lattice structures—a comparative study of As-built and hot isostatic pressed structures for medical implants. Met (Basel) Dec. 2022;12(12):2072. https://doi.org/10.3390/met12122072.
[51] M. Majeed, H.M. Khan, G. Wheatley, and R. Situ, "Influence of post-processing on additively manufactured lattice structures," 2022, *Springer Science and Business Media Deutschland GmbH*. doi:10.1007/s40430-022-03703-8.
[52] Park KM, Min KS, Roh YS. Design optimization of lattice structures under compression: study of unit cell types and cell arrangements. Mater (Basel) Jan. 2022;15(1):97. https://doi.org/10.3390/ma15010097.
[53] C. Pan, Y. Han, and J. Lu, "Design and optimization of lattice structures: a review," Sep. 02, 2020, *MDPI AG*. doi:10.3390/APP10186374.
[54] Schwahofer O, Büttner S, Colin D, Drechsler K. Tailored elastic properties of beam-based lattice unit structures. Int J Mech Mater Des 2023;19(4):927–49. https://doi.org/10.1007/s10999-023-09659-4.
[55] Joo HM, et al. Effect of cell geometry and heat treatment on the energy absorption property of AlSi10Mg alloy lattice structures produced by laser-based powder bed fusion. Met Mater Int 2024;30(5):1294–306. https://doi.org/10.1007/s12540-023-01567-8.
[56] Huang Y, Wang T, Nie G, Kang J, Yu H. A novel short-time heat treatment for stabilizing the compressive behavior of LPBF AlSi10Mg TPMS structures. J Alloys Compd 2025;1038:182675. https://doi.org/10.1016/j.jallcom.2025.182675.
[57] Nie Y, Tang Q, Zhao M, Song J. Effect of heat treatment on mechanical properties, failure modes and energy absorption characteristics of lattice skeleton and sheet structures fabricated by SLM. J Mater Res Technol 2023;26:4925–41. https://doi.org/10.1016/j.jmrt.2023.08.264.
[58] Jam A, Pellizzari M, Emanuelli L, Valsecchi G, du Plessis A, Benedetti M. Influence of heat treatment on the mechanical performance of Ti21S octet truss lattice structure fabricated by laser powder bed fusion. Prog Addit Manuf 2024;9(4):947–57. https://doi.org/10.1007/s40964-023-00494-9.
[59] Jin N, Yan Z, Wang Y, Cheng H, Zhang H. Effects of heat treatment on microstructure and mechanical properties of selective laser melted Ti-6Al-4V lattice materials. Int J Mech Sci 2021;190:106042. https://doi.org/10.1016/j.ijmecsci.2020.106042.
[60] Li D, Qin R, Xu J, Chen B, Niu X. Effect of heat treatment on AlSi10Mg lattice structure manufactured by selective laser melting: microstructure evolution and compression properties. Mater Charact 2022;187:111882. https://doi.org/10.1016/j.matchar.2022.111882.
[61] Caliskan M, Hafizoglu H, Babacan N. Dynamic mechanical properties of selective laser-melted AlSi10Mg lattice structures: experimental and numerical analysis with emphasis on Johnson-Cook model parameters. Int J Adv Manuf Technol 2024;132(7–8):3861–75. https://doi.org/10.1007/s00170-024-13570-3.
[62] Downing D, et al. Enhancing the energy absorption of AlSi10Mg thin-walled tubes with internal lattice structure through laser powder bed fusion. Prog Addit Manuf 2025;10(10):8557–76. https://doi.org/10.1007/s40964-025-01137-x.
[63] H. Yin, W. Zhang, L. Zhu, F. Meng, J. Liu, and G. Wen, "Review on lattice structures for energy absorption properties," 2023, *Elsevier Ltd*. doi:10.1016/j.compstruct.2022.116397.
[64] Wang Z, et al. Additively-manufactured 3D truss-lattice materials for enhanced mechanical performance and tunable anisotropy: simulations & experiments. Thin-Walled Struct 2023;183:110439. https://doi.org/10.1016/j.tws.2022.110439.
[65] Xiao L, Xu X, Feng G, Li S, Song W, Jiang Z. Compressive performance and energy absorption of additively manufactured metallic hybrid lattice structures. Int J Mech Sci 2022;219:107093. https://doi.org/10.1016/j.ijmecsci.2022.107093.
[66] Daynes S, Feih S. Functionally graded lattice structures with tailored stiffness and energy absorption. Int J Mech Sci 2025;285:109861. https://doi.org/10.1016/j.ijmecsci.2024.109861.
[67] Zhang P, Yu P, Zhang R, Chen X, Tan H. Grid octet truss lattice materials for energy absorption. Int J Mech Sci 2023;259:108616. https://doi.org/10.1016/j.ijmecsci.2023.108616.
[68] Qi D, et al. Mechanical behaviors of SLM additive manufactured octet-truss and truncated-octahedron lattice structures with uniform and taper beams. Int J Mech Sci 2019;163:105091. https://doi.org/10.1016/j.ijmecsci.2019.105091.
[69] Duport M, Martin G, Lhuissier P, Blandin JJ, Prima F, Dendievel R. Stabilizing post-yielding behavior of a stretching dominated lattice structure through microstructural optimization. Scr Mater 2022;219:114887. https://doi.org/10.1016/j.scriptamat.2022.114887.
[70] Yassine M, Almaskari F, Zaki W. Low-speed impact penetration characterization of sheet-based triply periodic minimal surfaces. Int J Mech Sci 2025;303:110561. https://doi.org/10.1016/j.ijmecsci.2025.110561.
[71] Xu P, et al. Crashworthiness analysis of the biomimetic lotus root lattice structure. Int J Mech Sci 2024;263:108774. https://doi.org/10.1016/j.ijmecsci.2023.108774.
[72] Chen SQ, Huang XY, Shuai LF, Wu GL, Huang TL, Huang XX. Annealing behavior of AlSi10Mg alloy fabricated by laser powder bed fusion. J Phys: Conf Ser Inst Phys 2023;2635:012036. https://doi.org/10.1088/1742-6596/2635/1/012036.
[73] Takata N, Kodaira H, Sekizawa K, Suzuki A, Kobashi M. Change in microstructure of selectively laser melted AlSi10Mg alloy with heat treatments. Mater Sci Eng: A 2017;704:218–28. https://doi.org/10.1016/j.msea.2017.08.029.
[74] Clement CD, Masson J, Kabir AS. Effects of heat treatment on microstructure and mechanical properties of AlSi10Mg fabricated by selective laser melting process. J Manuf Mater Process Jun. 2022;6(3):52. https://doi.org/10.3390/jmmp6030052.
[75] Zhou L, Mehta A, Schulz E, McWilliams B, Cho K, Sohn Y. Microstructure, precipitates and hardness of selectively laser melted AlSi10Mg alloy before and after heat treatment. Mater Charact 2018;143:5–17. https://doi.org/10.1016/j.matchar.2018.04.022.
[76] Aboulkhair NT, Tuck C, Ashcroft I, Maskery I, Everitt NM. On the precipitation hardening of selective laser melted AlSi10Mg. Met Mater Trans Phys Met Mater Sci 2015;46(8):3337–41. https://doi.org/10.1007/s11661-015-2980-7.
[77] Nurel B, Nahmany M, Frage N, Stern A, Sadot O. Split Hopkinson pressure bar tests for investigating dynamic properties of additively manufactured AlSi10Mg alloy by selective laser melting. Addit Manuf 2018;22:823–33. https://doi.org/10.1016/j.addma.2018.06.001.
[78] Tridello A, Boursier Niutta C, Benelli A, Paolino DS. Absorbing capabilities of additively manufactured lattice structure specimens for crash applications: damage tolerant design and simulations. Fatigue Fract Eng Mater Struct 2024;47(8):2730–51. https://doi.org/10.1111/ffe.14320.
[79] Boursier Niutta C, Paolino DS, Tridello A. Additively manufactured lattice structures: an innovative defect-based design methodology against crash impact. Eng Fail Anal 2023;152:107436. https://doi.org/10.1016/j.engfailanal.2023.107436.
[80] National Highway Traffic Safety Administration. Crash simulation vehicle models. Washington, DC, USA: U.S. Department of Transportation; 2025. Online]. Available: https://www.nhtsa.gov/crash-simulation-vehicle-models. accessed: Dec. 18.